

The role of phase transformation mechanism on the grain boundary network in a commercially pure titanium



Ehsan Farabi^a, Vahid Tari^b, Peter D. Hodgson^a, Gregory S. Rohrer^c, Hossein Beladi^{a,*}

^a Institute for Frontier Materials, Deakin University, Geelong, Victoria 3216, Australia

^b Eaton Corporation, Corporate Research & Technology, Southfield, MI 48076, USA

^c Department of Materials Science and Engineering, Carnegie Mellon University, Pittsburgh, PA 15213-3890, USA

ARTICLE INFO

Keywords:

Pure titanium

Phase transformation

Texture

Variant selection

Intervariant boundary plane character

distribution

ABSTRACT

The role of phase transformation mechanism on the development of the grain boundary network in a commercially pure Ti was investigated using five-parameter grain boundary analysis along with an analysis of the triple junctions among intervariant boundaries. High temperature β was subjected to three different cooling regimes (i.e., 175 °C/s, 1 °C/s and 0.02 °C/s) to stimulate shear, diffusion-assisted and pure diffusional β -to- α phase transformation mechanisms, resulting martensite, Widmanstätten, and coarse-grain microstructures, respectively. The phase transformation mechanism appeared to significantly alter the grain boundary network in pure Ti. There was a distinct difference in the misorientation angle distribution among microstructures formed through different phase transformation mechanisms, though the peaks were largely consistent with the Burgers orientation relationship. The $60^\circ/[1\ 1\ \bar{2}\ 0]$ intervariant boundary had the highest population ($\sim 60\%$) in the martensitic/shear transformation, because of a local variant selection mechanism (i.e., three variant clustering) influenced by the transformation strain. However, the local variant selection associated with the transformation strain gradually diminished with a decrease in the cooling rate, leading to a progressive decline in the $60^\circ/[1\ 1\ \bar{2}\ 0]$ population (i.e., the random distribution of intervariant boundaries). The $60^\circ/[1\ 1\ \bar{2}\ 0]$ intervariant boundary had symmetric tilt ($\bar{1}\ 1\ 0\ 1$) plane characteristics with a low energy configuration in the martensitic microstructure and an asymmetric tilt character in both diffusion-assisted and diffusional transformations. The three-variant clustering during the martensitic transformation significantly enhanced the connectivity of the $60^\circ/[1\ 1\ \bar{2}\ 0]$ intervariant boundaries at the triple junctions, though it became progressively less connected as the mechanism altered towards diffusion-assisted and diffusional phase transformations.

1. Introduction

Most attractive properties of titanium alloys arise from the complex structure of its major allotropic forms (i.e., α -hcp and β -bcc phases) achieved through different thermomechanical or heat treatment procedures [1,2]. Therefore, the $\beta \rightarrow \alpha$ phase transformation occurring during Ti processing has long been investigated, as it plays a crucial role on the texture development and microstructural characteristics [3–5]. The phase transformation in Ti alloys follows the Burgers orientation relationship (OR) [6] producing 12 distinct α variants from a given parent β grain. The presence of all or fewer α variants in the final microstructure has a direct impact on the transformation texture, and thus changes the final mechanical properties [2,7–10].

The preference in the nucleation of a given variant/s, known as variant selection, is commonly linked to specific mechanisms, which are related to the defect structures [11–14], prior β grain boundaries

[15–17] and the elastic anisotropy [18–20]. The introduction of crystal defects into the parent β phase, such as deformation twins [11] and dislocation structures [11,12,21] encourages a preferred α variant precipitation on the $(3\ 3\ \bar{2})[1\ 1\ 3]$ twin systems and the $\{1\ 1\ 2\}_\beta[1\ 1\ 1]_\beta$ slip systems, respectively. When the β grain boundary is the preferred nucleation site for α variants, the characteristics of a given β boundary (i.e., misorientation and grain boundary plane orientation) act as an important variant selection rule [17,22], which in fact alters the α -nucleation barrier energy (ΔG^*) [23,24]. In specific circumstances, similarly oriented α colonies are formed on a special β grain boundary, which maintain the Burgers OR with both adjacent β parent grains [16,17,25,26]. This appears as a thin layer of a specific α variant along the β boundary, which may dictate the orientation of side plates in the Widmanstätten microstructure of Ti alloys (i.e., limited number of variant formation on a given β grain; variant selection) [16,25,27]. This leads to the formation of textured regions in the vicinity of prior β

* Corresponding author.

E-mail address: hossein.beladi@deakin.edu.au (H. Beladi).

<https://doi.org/10.1016/j.matchar.2020.110640>

Received 30 July 2020; Received in revised form 1 September 2020; Accepted 11 September 2020

Available online 15 September 2020

1044-5803/ © 2020 Elsevier Inc. All rights reserved.

boundary known as “macrozones” [28,29]. On the other hand, the development of all 12 α variants is facilitated during high undercooling (e.g., the martensitic transformation), weakening the α overall texture [30,31]. However, the surge for accommodating the strain energy associated with the crystallographic shape change of the β -to- α transformation produces a local variant selection mechanism to maintain the material integrity [20,32,33]. The change in the variant selection mechanism for different processing routes is, therefore, expected to lead to different intervariant boundary characteristics that result from the intersection of distinct crystallographic variants during the $\beta \rightarrow \alpha$ phase transformation. This is an area which has received little consideration, despite the significant body of work dealing with the processing parameters affecting the variant selection mechanism/s through the phase transformation.

A recent boundary characterization breakthrough coupling conventional EBSD mappings with a stereological interpretation of the data [34] has made it possible to measure the distribution of all five independent crystallographic boundary parameters. This approach was successfully employed to measure the grain boundary character distribution for different alloys [35–39]. It has been demonstrated that the boundary plane character distribution is sensitive to the intrinsic (i.e., chemical composition [40,41] and the crystal structure [42–45]) and extrinsic (i.e., processing [46] and transformation routes [35,43]) parameters. Among different parameters, the impact of phase transformation on the grain boundary network has received limited attention, specifically for titanium alloys [20,37,39,47]. The recent work on the martensitic transformation in Ti alloys revealed that the crystallographic constraints associated with the phase transformation (rather than the plane interfacial energy) largely influence the characteristics of boundary plane orientation [31,48]. However, it is not clear to what extent the phase transformation path (i.e., variant selection mechanism) can alter the grain boundary network characteristics (i.e., plane orientation, population and connectivity) in Ti alloys.

The current study, therefore, aims to examine the role of phase transformation mechanisms (e.g., diffusional versus shear) on the intervariant boundary network characteristics in a commercially pure Ti. In the present work, the material was subjected to different phase transformation routes to obtain three distinct morphologies, namely coarse-grain, Widmanstätten and martensitic microstructures. The grain boundary network characteristics were then examined using the five-parameter grain boundary analysis along with an analysis of the triple junctions among intervariant boundaries. The former determined the grain boundary plane orientation for a given intervariant boundary and the latter analysed the boundary triple junctions as a function of intervariant boundary type arrangement. The current findings ultimately enable us to disclose novel ways to engineer the grain boundary network in Ti alloys through the phase transformation routine for specific application/s.

2. Experimental Procedure

2.1. Material

An extruded grade 2 commercially pure titanium alloy rod with an initial diameter of 20 mm was utilized for different heat treatment procedures. The as-received microstructure consisted of equiaxed grains with an average size of $10.9 \pm 0.1 \mu\text{m}$ (Fig. 1a). The extruded rod was initially machined to a diameter of 10 mm. Then, a 2 mm width line was machined through the length of extruded rod along the extrusion direction. This made it possible to align all processed samples along the same coordinates for the texture measurement. The samples with a dimension of 15 mm length and 10 mm diameter were machined from the extruded rod. They were then immersed in the dilute delta glaze to minimize the titanium oxidation at high temperatures during the heat treatment procedure. The samples were subjected to different heat treatment procedures using either a servo-testing machine, which

described in detail elsewhere [49], or a muffle furnace depending on cooling rate. The samples were initially reheated to 950 °C (i.e., the β -stable region) and held isothermally for 180 s in the servo-testing machine. They were then cooled through two different cooling rates, namely $\sim 175 \text{ }^\circ\text{C/s}$ (i.e., water-quenching, Fig. 2) and $1 \text{ }^\circ\text{C/s}$, resulting in martensitic and Widmanstätten microstructures, respectively. Another sample was heat treated in a muffle furnace at 950 °C for 3 min followed by furnace cooling (i.e., $\sim 0.02 \text{ }^\circ\text{C/s}$, Fig. 2) to room temperature, hereafter called the coarse-grain microstructure. To analyse the microstructure and texture changes taking place in α on heating, one sample was reheated to 850 °C (i.e., below α -to- β transformation temperature of 882 °C) at a rate of $5 \text{ }^\circ\text{C/s}$ followed by water-quenching (hereafter called the annealed microstructure) using the servo-testing machine.

2.2. Microstructural Characterization

The microstructure of heat-treated samples was examined using electron backscattered diffraction (EBSD). The samples were ground and polished using a $0.04 \mu\text{m}$ OPS suspension. The EBSD measurements were conducted using a FEG Quanta 3-D FEI SEM with the beam operated at 20 kV and 8 nA. TSL software was used to acquire the EBSD data using a hexagonal grid. For each heat treatment condition, multiple EBSD scans were executed (Table 1). The step size for the coarse-grain, Widmanstätten and martensitic microstructures was assigned to be $5 \mu\text{m}$, $3 \mu\text{m}$ and $0.3 \mu\text{m}$, respectively. The average confidence index for the coarse-grain and Widmanstätten microstructures were higher than 0.70 and for the martensitic microstructure was measured to be about 0.50. TSL OIM Analysis V6.1 software was used to perform the post-processing analysis on the EBSD data. First, the unclear data obtained through the EBSD measurements were cleaned using the grain dilation function. Then, the neighbouring pixel groups with a similar orientation (less than 5°) were related to one single grain by applying the single average orientation function. Finally, the boundary line traces/segments were extracted by the reconstructed grain boundary function and a boundary deviation limit of 2 pixels (e.g., $2 \times 0.3 \mu\text{m}$ step size = $0.6 \mu\text{m}$). The obtained boundary segments were used to measure the intervariant boundary plane character distribution through an automated stereological approach, which is described in detail elsewhere [34]. To reliably determine the grain boundary plane distribution in a material with hexagonal symmetry, around 200,000 grain boundary line segments are required [50]. Although acquiring this amount of segments can be obtained in a reasonable time frame for the fine martensitic structure, for the slower cooling rates with coarse microstructures this can be difficult to conduct in a timely manner. As discussed later, the crystallographic constraints associated with the $\beta \rightarrow \alpha$ phase transformation resulted in the formation of interfaces with a few nearly discrete misorientations. Because all of the observations are clustered at these misorientations (rather than being spread over all possibilities), it is possible to reliably measure the grain boundary plane orientation distribution at these specific misorientations with a smaller number of boundary line segments; here with use approximately 100,000 boundary segments. The measurement was conducted with 9 bins per 90° , providing 10° resolution. Moreover, the EBSD measurements were conducted on two perpendicular surfaces (i.e., parallel and perpendicular cross sections to the extruded axis of samples) for all microstructures to reduce the texture bias in the distribution of intervariant boundary planes. The measured EBSD area and number of boundary segments were summarised in Table 1 for each heat treatment condition. It should be emphasised that some of the data related to the martensitic microstructure was already presented in [46]. In parallel, the connectivity of the grain boundary network was characterized using the triple junction analysis. In this approach, the grain boundary triple junctions were classified as a function of a specific boundary type (i.e., a given lattice misorientation). Here, the classification was only performed for the intervariant boundaries associated

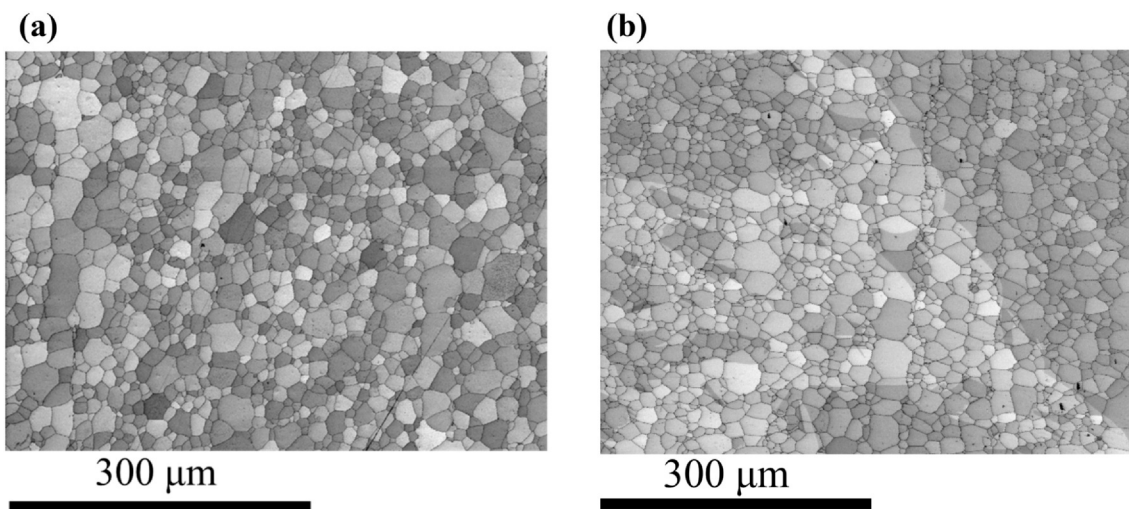


Fig. 1. the image quality map of the (a) as-received condition and, (b) the annealed sample.

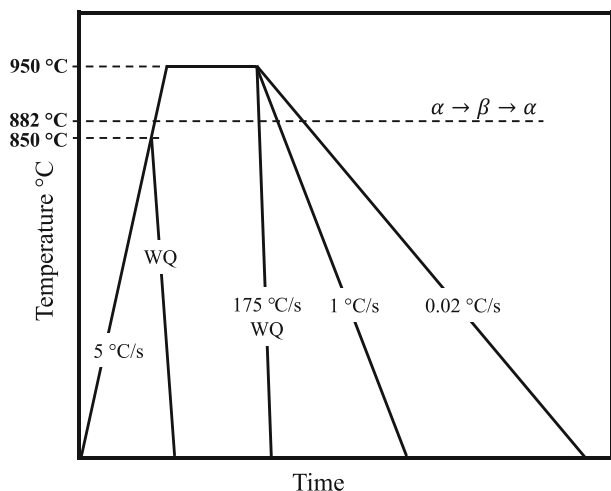


Fig. 2. Schematic illustration of the heat treatment procedure in this study.

with the $\beta \rightarrow \alpha$ phase transformation following the Burgers OR, since their total length fraction was more than 96%, as shown later. A thorough description of the triple junction analysis is mentioned in reference [51].

2.3. Texture

To measure the overall texture, multiple EBSD maps were recorded for samples subjected to all heat treatment conditions except the coarse-grain microstructure, using a Zeiss LEO 1530 field-emission gun SEM operated at 20 kV. The detail of EBSD measurements were summarised in Table 1. The data post-processing was conducted using HKL Channel 5 software. The texture of coarse-grain microstructure was measured

Table 1

The EBSD conditions for grain boundary and texture measurements of the martensitic, Widmanstätten, coarse-grain and annealed microstructures.

Microstructure	Grain boundary measurements			Texture measurements	
	Step size (μm)	EBSD area	Line segments	Step size (μm)	EBSD area
Martensite	0.3	$14 \times 250\mu\text{m} \times 250\mu\text{m}$	$\sim 2,000,000$	30 μm	$30 \times 4.17\text{mm} \times 3.12\text{mm}$
Widmanstätten	3	$34 \times 1500\mu\text{m} \times 1500\mu\text{m}$	$\sim 100,000$	30 μm	$52 \times 4.17\mu\text{m} \times 3.12\mu\text{m}$
Coarse-grain	5	$210 \times 2400\mu\text{m} \times 2400\mu\text{m}$	$\sim 100,000$	Same ^a	Same ^a
Annealed	–	–	–	30 μm	$10 \times 4.17\text{mm} \times 3.12\text{mm}$

^a The texture measurements data used from the same EBSD maps obtained for the grain boundary measurements.

using the EBSD maps obtained for the grain boundary measurement (Table 1).

3. Results

3.1. Texture Evolution

The (0 0 0 1) pole figure of the as-received material revealed a basal fibre texture (i.e., ~ 6.18 multiples of random distribution (MRD), Fig. 3a), spreading from the normal direction (ND) towards the transverse direction (TD). On the other hand, the (1 0 $\bar{1}$ 0) and (1 1 $\bar{2}$ 0) pole figures displayed a moderate peak mostly centred at ED with an intensity of ~ 3 MRD. After reheating to the 850 °C, the (0 0 0 1) pole figure showed a centralized peak at the ND position perpendicular to the extrusion direction with a significantly higher intensity (i.e., ~ 10 MRD, Fig. 3b). The a-axis became uniformly spread around the ED and TD directions with a peak intensity more or less similar to the as-received condition (i.e., ~ 3 MRD).

The overall texture for different $\beta \rightarrow \alpha$ phase transformation routes was qualitatively similar to both annealed and as-received conditions (Figs. 3 and 4). However, the overall texture intensity was significantly affected by the cooling rate, as it progressively increased in the (0 0 0 1) pole figure from ~ 5.0 MRD for the water-quenched condition to ~ 14.6 MRD for the slow-cooled (i.e., coarse-grain) condition (Fig. 4a-c). Interestingly, the (1 0 $\bar{1}$ 0) and (1 1 $\bar{2}$ 0) pole figures were also influenced by the cooling rate (i.e., transformed products). In the water-quenched sample, a strong peak existed with an intensity of ~ 5.7 MRD about the ED position in the (1 1 $\bar{2}$ 0) pole figure (Fig. 4a), while the intensity decreased to ~ 3.8 MRD in the air-cooled condition (Fig. 4b). On the other hand, the slow-cooled/coarse-grain condition revealed multiple peaks in the (1 1 $\bar{2}$ 0) pole figure with a moderate intensity of ~ 5 MRD slightly deviated from ED towards ND (Fig. 4c). The slow-cooled condition also displayed a strong peak with an intensity of ~ 10 MRD,

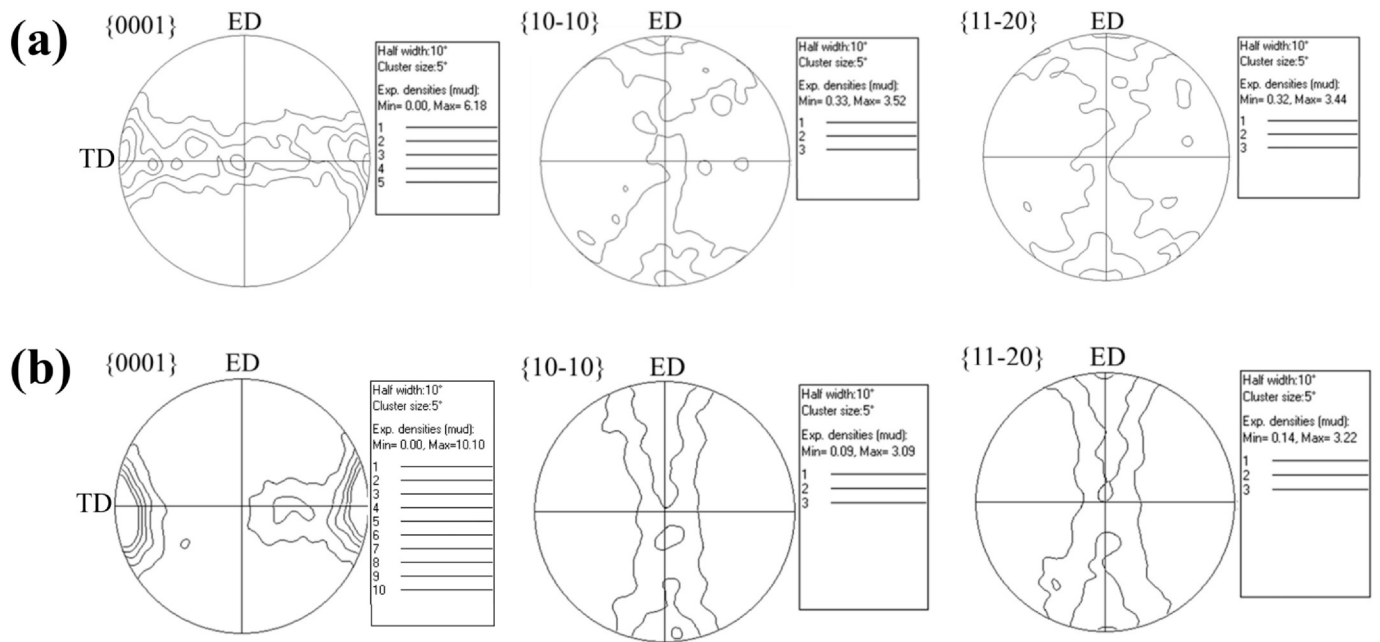


Fig. 3. The corresponding pole figures of (a) as-received and (b) annealed conditions.

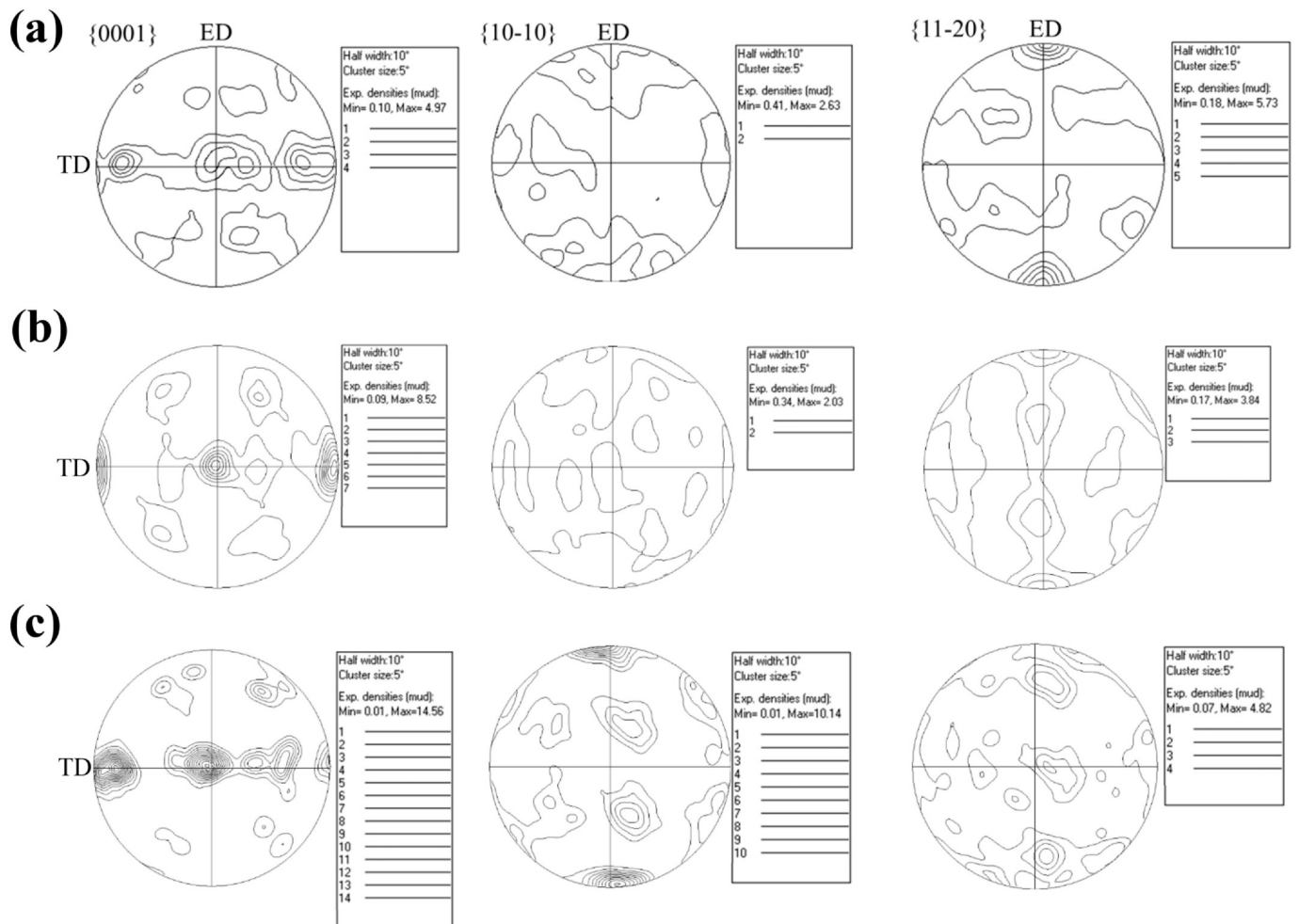


Fig. 4. The transformation pole figures for (a) martensitic, (b) Widmanstätten and (c) coarse-grain (slow-cooled) microstructures.

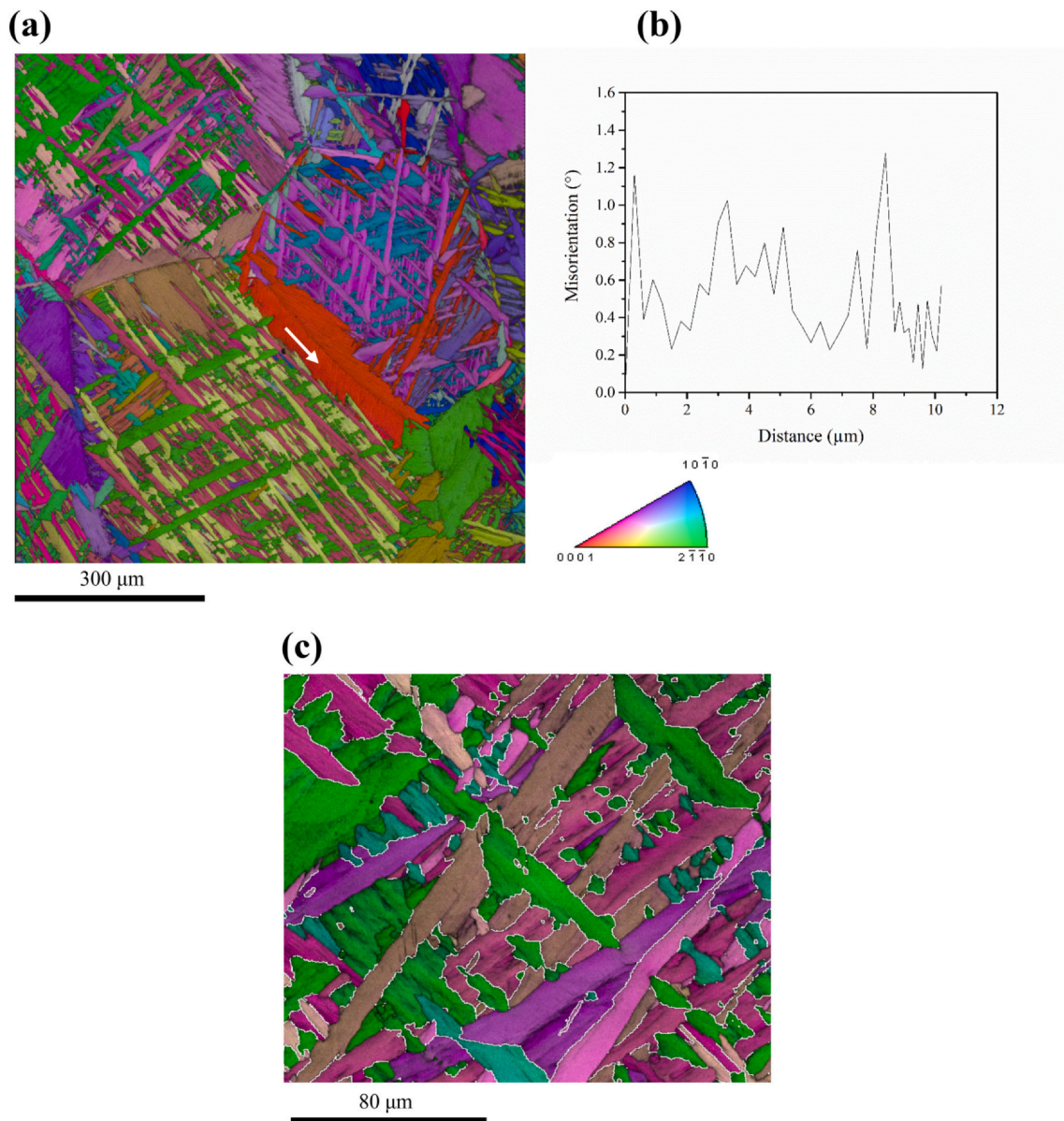


Fig. 5. (a) The image quality (IQ) map of the martensite microstructure and the (0001) poles corresponding two separated parallel variants, (b) the misorientation evolution along the white arrow in (a), (c) V-shape variants, parallel laths and three variant clusters of martensite deviated by $60^\circ [1\ 1\ \bar{2}\ 0]$ and separated by white lines.

which appeared about the ED position in the $(10\ \bar{1}\ 0)$ pole figure (Fig. 4a), while showing a significant weakening of this peak to ~ 2 MRD for the air-cooled and ~ 2.6 MRD for the water-quenched conditions, respectively (Figs. 4b and c).

3.2. Microstructural Observations

A change in the cooling rate resulted into three distinct microstructures, namely: i) the martensitic microstructure showing relatively thin martensite laths with an average thickness size of $1.95 \pm 0.02\ \mu\text{m}$ (Fig. 5), which were mostly confined within a narrow region in the vicinity of surface of the water-quenched sample due to the low heat conductivity of pure titanium [52], ii) Widmanstätten microstructure consisted of coarse patches of α (i.e., an average size of $71 \pm 5\ \mu\text{m}$ surrounded by irregular and serrated boundaries formed at a moderate cooling rate of $1\ \text{°C/s}$ (Fig. 6), and iii) coarse-grain microstructure with an average grain size of $129 \pm 38\ \mu\text{m}$ formed through a very slow cooling rate of $0.02\ \text{°C/s}$ (Fig. 7).

The martensitic microstructure consisted of fine laths, arranged in two distinct morphologies. The first morphology appeared as elongated packets of parallel aggregates/laths separated either by low (i.e., lower than 5° depicted by a white arrow in Fig. 5a and b) or high misorientation angle boundaries (i.e., having $60^\circ [1\ 1\ \bar{2}\ 0]$ misorientation, Fig. 5c). The second morphology was a set of laths forming a triangular shape or V-shape variant arrangement, also separated by $60^\circ [1\ 1\ \bar{2}\ 0]$ misorientation. These large triangles were filled with smaller triangles and separated by the $60^\circ [1\ 1\ \bar{2}\ 0]$ misorientation (Fig. 5a and c).

The microstructure cooled at $1\ \text{°C/s}$ had a relatively thicker α -lath structure than the martensitic condition, consisting of parallel aggregates with very close orientations (i.e., white arrow in Figs. 6a and b), hereafter called Widmanstätten α -grains. A triangular morphology was occasionally observed within the Widmanstätten microstructure (Figs. 5c and d), being separated either by $60^\circ [1\ 1\ \bar{2}\ 0]$ similar to martensite (Figs. 5c and 7d) or different high angle boundaries (Fig. 6c). For the slow-cooled condition, the microstructure was very coarse and grains had an elongated morphology. It appeared that each

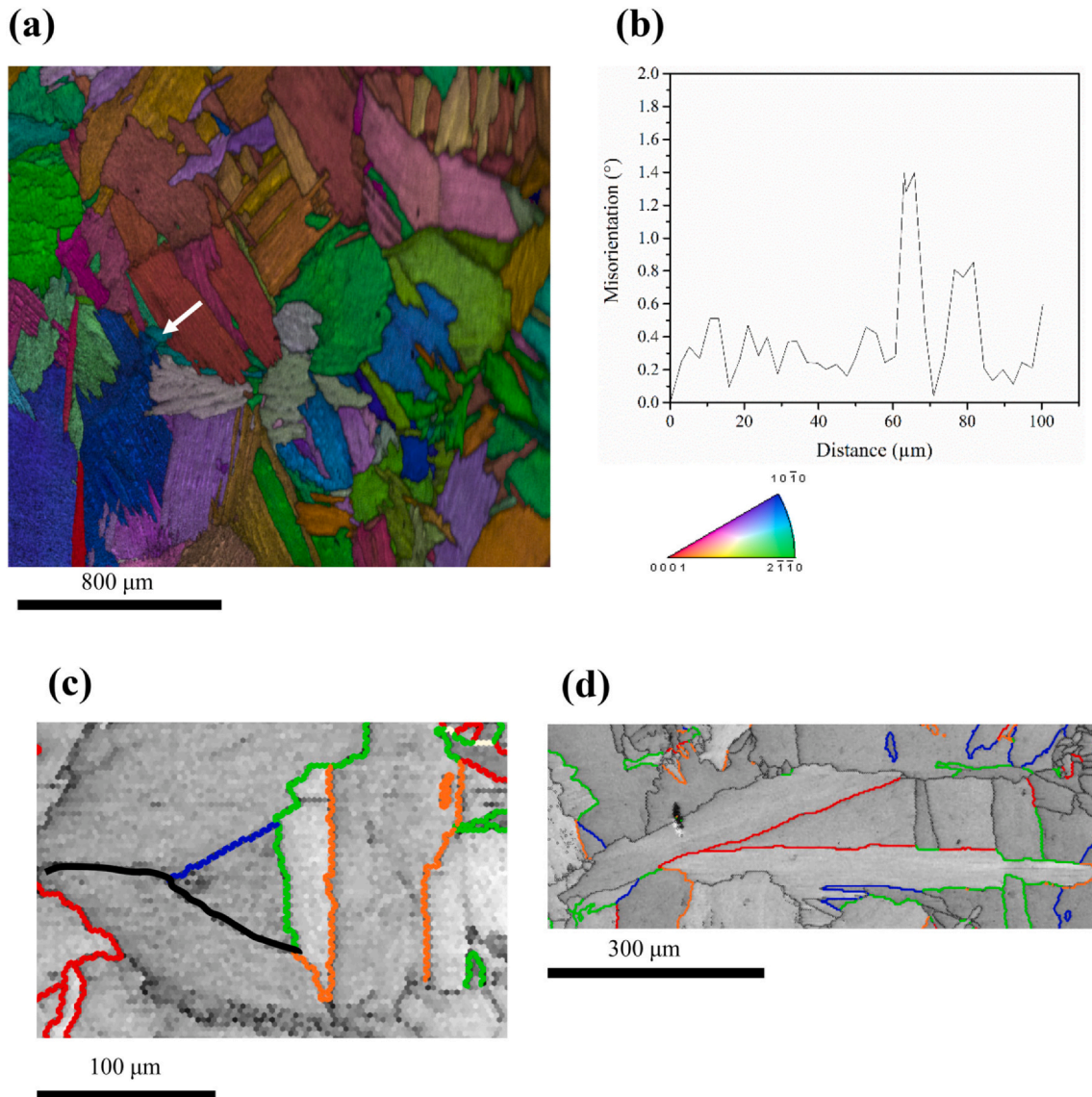


Fig. 6. (a) The image quality (IQ) and IPF map of Widmanstätten microstructure, (b) the point to point misorientation evolution along the white arrow in (a), (c) and (d) The boundary map of the two triangular morphologies. Here the red, green, blue and orange lines indicate the $60^\circ/[1\ 1\ \bar{2}\ 0]$, $60.83^\circ/[\bar{1}.377\ \bar{1}\ 2.377\ 0.359]$, $63.26^\circ/[\bar{1}0\ 5\ 5\ \bar{3}]$ and $90^\circ/[1\ 2.38\ 1.38\ 0]$, respectively. The black line represent boundaries lower than 2° . (For interpretation of the references to colour in this figure legend, the reader is referred to the web version of this article.)

grain was made of parallel α -aggregates separated by low misorientation angles of less than 2° (Figs. 7a and b).

3.3. Intervariant Boundary Distribution

In theory, the $\beta \rightarrow \alpha$ phase transformation follows the Burgers orientation relationship (Burgers OR) [6] where the close packed planes and the nearest neighbour direction for the parent (β -bcc) and the daughter phase (α -hcp) are parallel (i.e., the $\{1\ 1\ 0\}_\beta$ and $\{0\ 0\ 0\ 1\}_\alpha$ planes and $\langle 1\ 1\ 1 \rangle_\beta$ and $\langle 1\ 1\ \bar{2}\ 0 \rangle_\alpha$). Based on this orientation relationship, the $\beta \rightarrow \alpha$ phase transformation results in the formation of 12 distinct α -variants and their intersections produces 5 distinct intervariant boundaries [53] (Table 2). Interestingly, the grain boundary misorientation angle distribution revealed multiple peaks at positions (i.e., angles of $\sim 10^\circ$, $55\text{--}65^\circ$ and $\sim 90^\circ$) close to the lattice misorientation angle/axis expected from the Burgers OR in all transformed microstructures (Fig. 8 and Table 2). This suggests that the Burgers OR was closely followed for all transformation mechanisms. The position of main peak/s appearing in the range of $55\text{--}65^\circ$ was qualitatively similar

for all phase transformation mechanisms, though the peak/s differed significantly in intensity (Fig. 8). As discussed later, the approximate parent β phase grain size was estimated to be in a range of $600\text{--}800\ \mu\text{m}$ by considering the spacing of grain boundaries, which were not related to the Burgers orientation relationship (i.e., $< 7.5^\circ$, $12.5\text{--}57.5^\circ$, $65\text{--}87.5^\circ$).

The length fraction of intervariant boundaries was calculated for each phase transformation path and depicted in Fig. 9. Overall, the measured fractions showed a significant discrepancy from the theoretically calculated values for all phase transformation mechanisms. In addition, the intervariant boundary length fraction was considerably affected by the phase transformation mechanism. The martensitic phase transformation had the $60^\circ/[1\ 1\ \bar{2}\ 0]$ as the dominant intervariant boundary sharing about 60% of the length fraction. On the other hand, the $10.53^\circ/[0001]$, $60.83^\circ/[\bar{1}.377\ \bar{1}\ 2.377\ 0.359]$, $63.85^\circ/[\bar{1}0\ 5\ 5\ \bar{3}]$ and $90^\circ/[1\ 2.38\ 1.38\ 0]$ intervariants had populations of $\sim 2\%$, 12% , 13% and 5% , respectively. For the Widmanstätten microstructure, the intervariant boundaries with the highest length fractions were $60.83^\circ/[\bar{1}.377\ \bar{1}\ 2.377\ 0.359]$ ($\sim 29\%$) and $63.85^\circ/[\bar{1}0\ 5\ 5\ \bar{3}]$ ($\sim 21\%$). The other

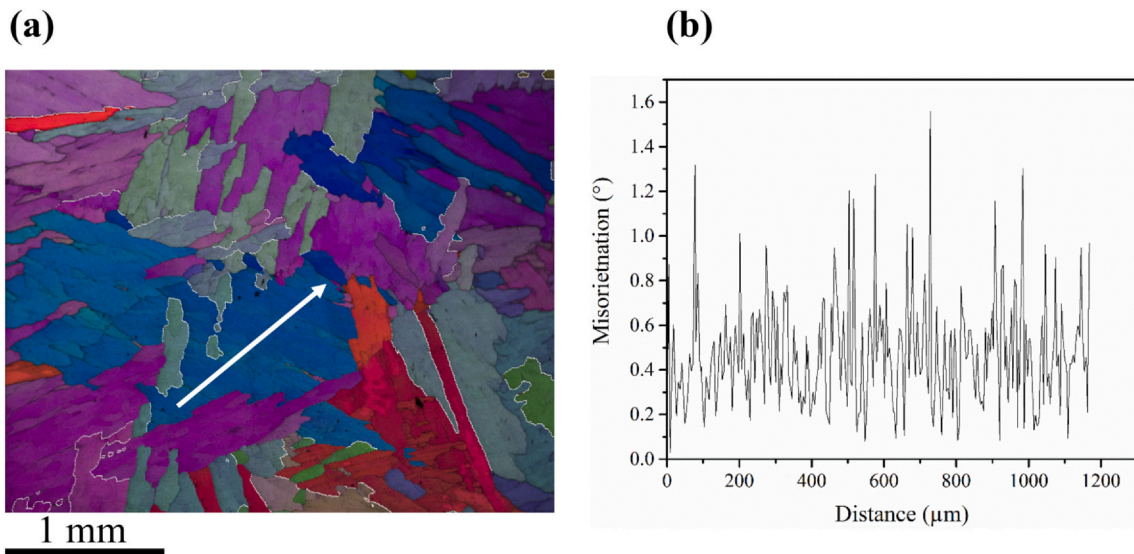


Fig. 7. a) The image quality (IQ) map of slow-cooled microstructure and, (b) the misorientation distribution of the white arrow in between parallel laths,

Table 2
Individual variants of Burgers OR corresponding to the β matrix and the α product phase [53].

Variants	Orientation relationship	Intervariant boundary (from V_1)
1	$(1\bar{1}0)_\beta // (0001)_\alpha, [111]_\beta // [11\bar{2}0]$	–
2	$(10\bar{1})_\beta // (0001)_\alpha, [111]_\beta // [11\bar{2}0]$	$[11\bar{2}0]/60^\circ$
3	$(01\bar{1})_\beta // (0001)_\alpha, [111]_\beta // [11\bar{2}0]$	$[11\bar{2}0]/60^\circ$
4	$(110)_\beta // (0001)_\alpha, [\bar{1}11]_\beta // [11\bar{2}0]$	$[1\bar{2}38\bar{1}38\ 0]/90^\circ$
5	$(101)_\beta // (0001)_\alpha, [\bar{1}11]_\beta // [11\bar{2}0]$	$[\bar{1}0\ 5\ 5\ \bar{3}]/63.26^\circ$
6	$(01\bar{1})_\beta // (0001)_\alpha, [\bar{1}11]_\beta // [11\bar{2}0]$	$[\bar{1}.377\ \bar{1}\ 2.377\ 0.359]/60.83^\circ$
7	$(110)_\beta // (0001)_\alpha, [1\bar{1}1]_\beta // [11\bar{2}0]$	$[1\bar{2}38\bar{1}38\ 0]/90^\circ$
8	$(10\bar{1})_\beta // (0001)_\alpha, [1\bar{1}1]_\beta // [11\bar{2}0]$	$[\bar{1}.377\ \bar{1}\ 2.377\ 0.359]/60.83^\circ$
9	$(011)_\beta // (0001)_\alpha, [1\bar{1}1]_\beta // [11\bar{2}0]$	$[\bar{1}0\ 5\ 5\ \bar{3}]/63.26^\circ$
10	$(1\bar{1}0)_\beta // (0001)_\alpha, [11\bar{1}]_\beta // [11\bar{2}0]$	$[0\ 0\ 0\ 1]/10.53^\circ$
11	$(101)_\beta // (0001)_\alpha, [11\bar{1}]_\beta // [11\bar{2}0]$	$[\bar{1}.377\ \bar{1}\ 2.377\ 0.359]/60.83^\circ$
12	$(011)_\beta // (0001)_\alpha, [11\bar{1}]_\beta // [11\bar{2}0]$	$[\bar{1}.377\ \bar{1}\ 2.377\ 0.359]/60.83^\circ$

intervariant boundaries totalled about ~11%, 16% and 15% for $10.53^\circ/[0\ 0\ 0\ 1]$, $60^\circ/[1\ 1\ \bar{2}\ 0]$ and $90^\circ/[1\ \bar{2}38\bar{1}38\ 0]$, respectively. Interestingly, the $60.83^\circ/[\bar{1}.377\ \bar{1}\ 2.377\ 0.359]$ (~32%) and the $60^\circ/[1\ 1\ \bar{2}\ 0]$ (~23%) intervariant boundaries were the most populated ones for the coarse-grain microstructure and the $10.53^\circ/[0\ 0\ 0\ 1]$, $63.85^\circ/[\bar{1}0\ 5\ 5\ \bar{3}]$ and $90^\circ/[1\ \bar{2}38\bar{1}38\ 0]$ had length fractions of about ~9%, 17% and 13%, respectively.

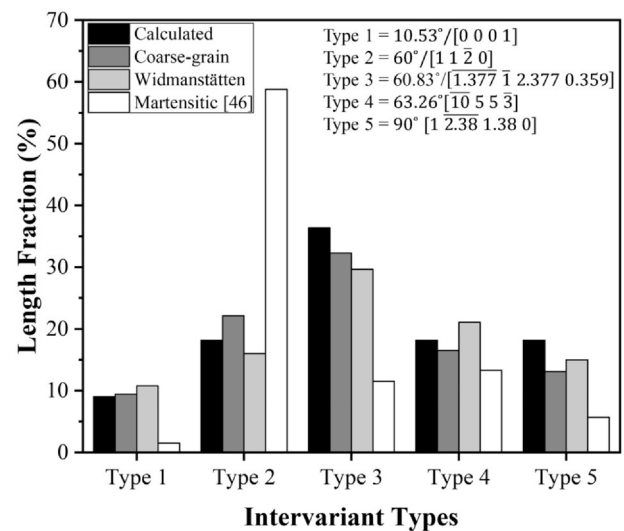


Fig. 9. The length fraction of grain boundaries associated with the Burgers orientation relationship (i.e., intervariant boundary population) for different microstructures. The intervariant between the V_1 and V_i ($i = 2-12$) has been indicated in Table 6. The theoretically calculated fractions is based on the assumption of all variants having equal statistical probability during phase transformation [20]. The “=” sign shows equivalent intervariant interfaces

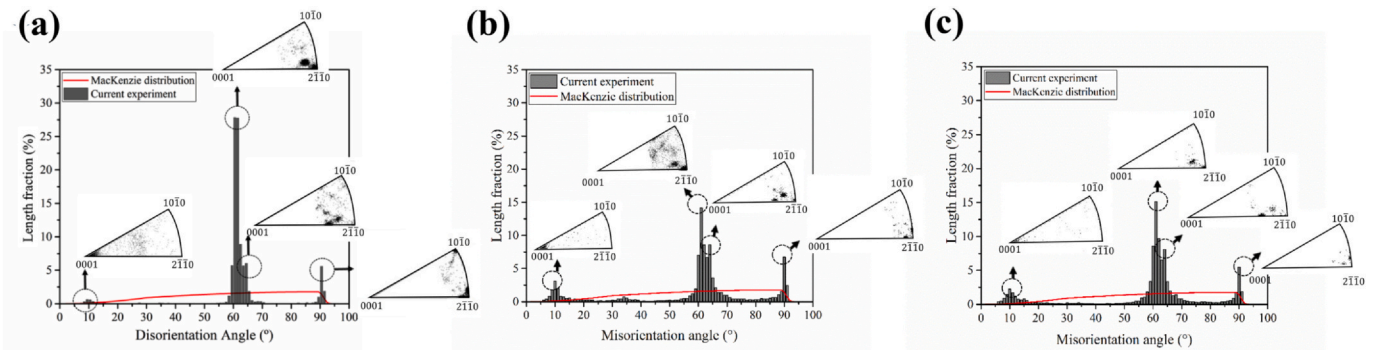


Fig. 8. The misorientation angle distribution of (a) martensitic from ref. [46], (b) diffusion-assisted, (c) diffusion transformation paths. The red line is the distribution for a Ti alloy with random texture. (For interpretation of the references to colour in this figure legend, the reader is referred to the web version of this article.)

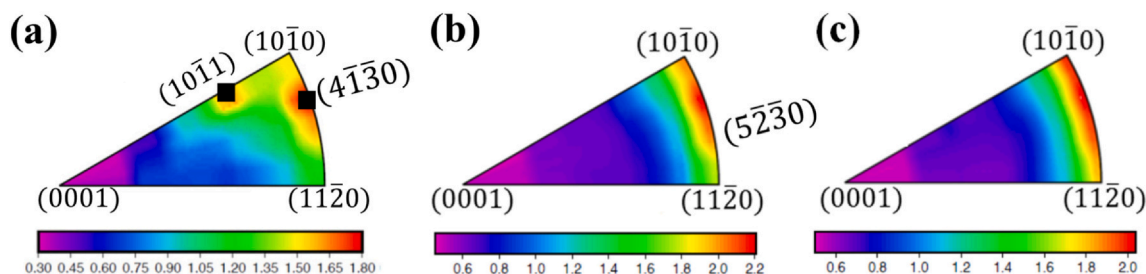


Fig. 10. The distribution of grain boundary planes depicted in the fundamental zone for all misorientations in (a) martensite from ref. [46], (b) Widmanstätten and (c) coarse-grain microstructures.

In total, the intervariant population for the Widmanstätten and coarse-grain samples were much closer to the one expected from the theoretical Burgers OR in comparison to the martensitic microstructure. The length fractions of boundaries misoriented by more than 5° from a Burgers OR were $\sim 6.58\%$, 7.55% and 9.72% for coarse-grain, Widmanstätten and martensite microstructures, respectively.

3.4. Intervariant Boundary Plane Distribution

The intervariant boundary plane distributions for the three samples, which show the relative areas of boundary planes for all misorientations, are plotted in a stereographic projection (Fig. 10). The distribution for the martensitic microstructure was significantly different from the coarse-grain and Widmanstätten samples. The overall intensity of the intervariant boundary plane distribution for the martensite was ~ 1.62 MRD (i.e., 62% more than expected for a random distribution) centred around two main peaks. The first peak was positioned at a prismatic plane orientation of $\{4\bar{1}30\}$. The second peak appeared at the position of the pyramidal $\{10\bar{1}1\}$ orientation (Fig. 10a). For the Widmanstätten, the maximum intensity was ~ 2.2 MRD (i.e., 120% more than a random distribution), spreading from $\{10\bar{1}0\}$ towards $\{5\bar{2}30\}$ (Fig. 10b). The coarse-grain had a maximum that spread between $\{10\bar{1}0\}$ and $\{11\bar{2}0\}$ having a maximum intensity of ~ 2.1 MRD (Fig. 10c). Interestingly, the minimum was positioned at the $\{0001\}$ planes for all microstructures (Fig. 10).

The aforementioned misorientation angle distributions for the transformed microstructures were clustered around theoretical misorientations expected from Burgers OR (Fig. 8). This specific misorientation angle distribution makes it possible to measure the distribution of boundary plane orientations at certain misorientations that are over represented in the distribution. To confirm this, the boundary planes character distribution for $60^\circ/[11\bar{2}0]$ misorientation was measured for 10,000, 40,000, 80,000 and 100,000 boundary segments of the coarse grain microstructure (Fig. 11). In the distribution, the $\{0001\}$ basal plane was placed in the centre while the prismatic planes (i.e. $\{11\bar{2}0\}$ and $\{10\bar{1}0\}$) were located at the circumference of stereogram. It was observed that the boundary plane peak position was clustered around a specific orientation for all boundary segments and its intensity remained nearly constant above 80,000 boundary line segments (Fig. 11c). Therefore, 100,000 boundary line segments could safely be used to reliably calculate the boundary planes character distribution in the current study.

The distributions of intervariant planes for specific lattice misorientations associated with the Burgers orientation relationship are plotted in Fig. 12. The characteristic boundaries associated with each intervariant boundary were also derived using the Glowinski's grain boundary toolbox software [54]. For the martensitic microstructure, the $10.53^\circ/[0001]$ intervariant included only $\sim 2\%$ of total boundary length fraction (Fig. 9). Therefore, its distribution was not considered significant. However, boundaries with this misorientation accounted for more than 10% of total population for the Widmanstätten and coarse-grain microstructures, which made the measurements

meaningful. The $10.53^\circ/[0001]$ intervariant boundary plane had a diffuse peak around prismatic planes and mostly clustered around $\{91\bar{1}0\}$ and $\{7\bar{3}40\}$ tilt/twist orientations with an intensity of ~ 2.7 and 2.4 MRD for the Widmanstätten and coarse-grain microstructures, respectively (Figs. 12b and c).

For the $60^\circ/[11\bar{2}0]$ misorientation, the distribution of intervariant boundary planes in the martensitic structure revealed a sharp peak with an intensity of ~ 500 MRD around the $(\bar{1}101)$ orientation having an ideal symmetric tilt/twist character (Fig. 12d and Table 3). The maximum was reduced significantly with a decrease in the cooling rate to ~ 89 MRD and ~ 96 MRD for Widmanstätten and coarse-grain microstructures, respectively (Figs. 12e and f). In addition, the distributions for Widmanstätten and coarse-grain microstructures revealed no specific peak and the maxima were spread along the tilt boundary planes (i.e., asymmetric tilt character) from the $(\bar{1}100)$ prismatic to the (0001) basal planes (Figs. 12e and f).

The intervariant boundary plane distribution for the $60.83^\circ/[1\bar{1}377\bar{1}2.3770.359]$ showed a rather similar distribution for all transformed microstructures (Figs. 12g-i). The distribution displayed a peak around the (4310) orientation with an intensities of ~ 14 , ~ 39 and ~ 26 MRD for martensite, Widmanstätten and coarse-grain microstructures, respectively (Figs. 12g-i). This peak deviates from the $(\bar{3}320)$ tilt boundary character by 9° (Table 3). The distribution of the intervariant boundary planes for the $63.26^\circ/[1055\bar{3}]$ misorientation was qualitatively similar for all transformation paths showing a strong peak around the $(\bar{3}210)$ plane (Figs. 12j-l), which had the twist characteristics. However, the distribution intensity differed significantly as the maxima were ~ 204 , 235 and 153 MRD for the martensitic, Widmanstätten and coarse-grain microstructures, respectively.

The distribution of intervariant boundary planes character for the $90^\circ/[1\bar{2}381.380]$ misorientation revealed a sharp peak around $(1\bar{1}01)$ orientation with a maximum of ~ 60 MRD, having the quasi-symmetric twist character (Fig. 12m and Table 3). However, the Widmanstätten microstructure revealed multiple peaks, with an intensity of ~ 63 MRD, around $(3\bar{2}\bar{1}0)$ and $(1\bar{2}13)$ orientations deviated by 6° and 10° from $(7\bar{4}30)$ and $(1\bar{2}12)$ tilt boundaries, respectively (Fig. 12n and Table 3). The grain boundary plane distribution for the coarse-grain microstructure had a spread peak along $(3\bar{2}\bar{1}0)$ and $(1\bar{2}13)$ orientations with an intensity of ~ 31 MRD (Fig. 12o).

3.5. Grain Boundary Network Connectivity

Fig. 13 shows the number fraction of different classes of triple junctions for all five types of intervariant boundaries in martensite, Widmanstätten and coarse-grain microstructures. Total numbers of 35,530, 1644 and 850 triple junctions were detected in the martensitic, Widmanstätten and coarse-grain microstructures, respectively. For the martensitic microstructure, the number fraction of triple junctions consisting of three $60^\circ/[11\bar{2}0]$ intervariant boundaries (i.e. class 3) was high (53%) and only 6% of the triple junction did not contain any $60^\circ/[11\bar{2}0]$ boundary (i.e. class 0, Fig. 13a). The other intervariant boundary types largely belonged to the class 1 triple junction in the

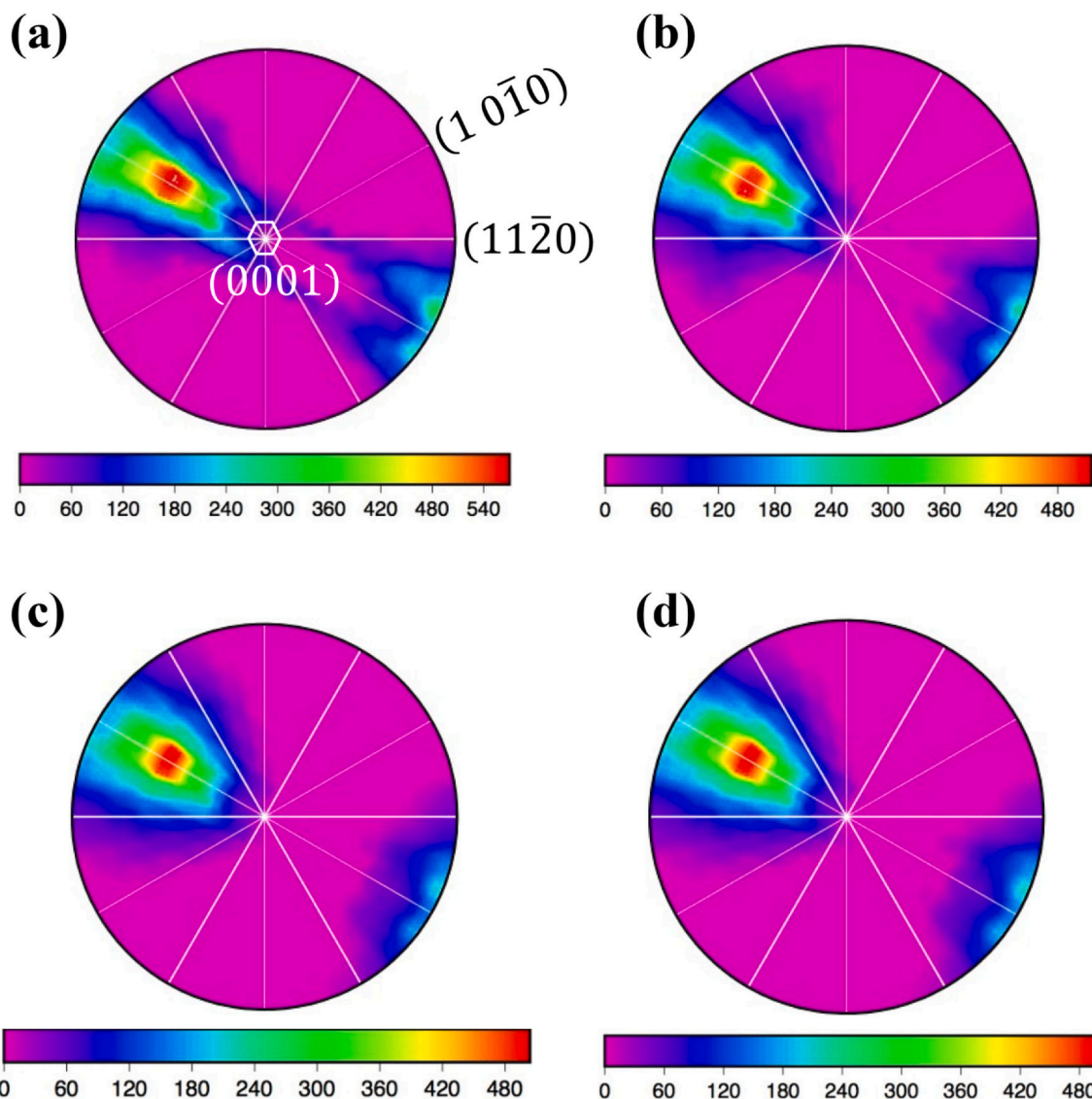


Fig. 11. The grain boundary plane distribution for the $60^\circ/[1\ 1\ \bar{2}]$ misorientation of (a) $\sim 10,000$, (b) $\sim 40,000$, (c) $\sim 80,000$ and (d) $\sim 100,000$ boundary segments in the martensite microstructure. All the intensities are described in multiples of random distribution (MRD).

martensite, though type 1 intervariant boundaries ($10.53^\circ/[0001]$) had the smallest frequency (Fig. 13a). With an increase in the cooling rate, the class 3 triple junction frequency for the type 2 intervariant boundary significantly reduced to 5% and 3% for the Widmanstätten and coarse-grain microstructures, respectively (Fig. 13). However, a decrease in the cooling rate resulted in a weak presence of other types of intervariant boundaries in class 3 and 2 triple junction categories. In general, the frequency of class 1 triple junction was enhanced for most intervariant boundary types with increasing cooling rate (Fig. 13).

4. Discussion

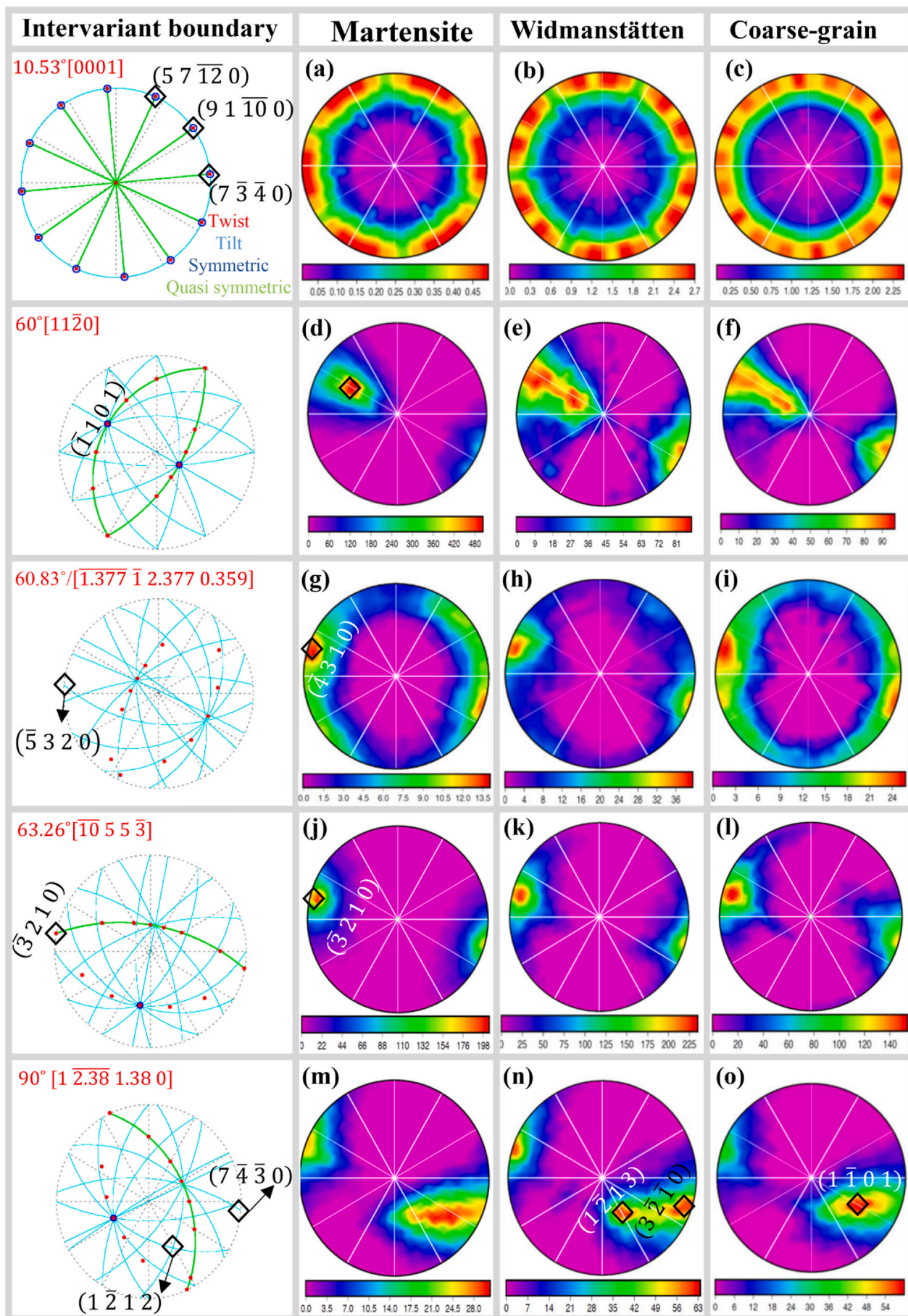
The current results reveal that the phase transformation mechanism significantly alters the overall texture (Fig. 3), microstructure and grain boundary network characteristics (i.e., population, plane orientation and connectivity, Figs. 8, 9, 10, 12 and 13). These changes can be attributed to the mechanism and extent of variant selection occurring during different phase transformation routes.

4.1. Transformation Texture and Variant Selection

The governing Burgers OR [6] in the $\alpha \leftrightarrow \beta$ phase transformation

theoretically leads to the formation of six distinct β variants from a given α parent grain during reheating ($\alpha \rightarrow \beta$) and twelve possible α -orientations from a single β grain upon cooling ($\beta \rightarrow \alpha$). Accordingly, if the formation of all variants takes place with the same probability, a relatively weak overall texture is expected upon the transformation. However, titanium alloys are known for their tendency to preserve their texture components during $\alpha \leftrightarrow \beta$ phase transformation (i.e., known as texture memory effect [26,55]), which is widely related to the preference of specific variant/s forming during the phase transformation [3,4,7,56,57]. However, the current observation reveals that the phase transformation mechanism significantly alters the resultant overall texture, being different from the as-received condition.

During reheating to 850°C , the α overall texture significantly changed, showing a pronounced peak about TD, prior to the $\alpha \rightarrow \beta$ phase transformation (Fig. 3b). This distinct change can be related to α grain growth and/or α recrystallization [58,59]. As the α grain size largely appears similar to the as-received condition (i.e., grain size of $\sim 11.2 \pm 0.1\ \mu\text{m}$ for the annealed sample, Figs. 1a and b), it suggests that the change in α overall texture is mainly due to the recrystallization process occurring upon reheating. Therefore, if the texture memory fully takes place during the $\beta \rightarrow \alpha$ phase transformation on cooling, the α overall phase transformation texture is expected to be largely similar



(caption on next page)

Fig. 12. Distribution of intervariant interface/boundary planes character for different intervariants and the corresponding calculated geometrically characteristic boundaries for different phase transformation paths. (d), (g), (j) and (m) are from ref. [46].

to the recrystallized α texture. However, a distinct α overall texture is observed for each phase transformation path, which is different from the α recrystallized texture. This can be explained through the variant selection mechanisms and/or the possible β grain growth taking place on reheating above $\alpha \rightarrow \beta$ transient temperature (i.e., 890 °C). In the pure Ti alloy, the β grain growth is inevitable due to the absence of alloying elements, and a relatively coarse β grain is obtained as a result of reheating at 950 °C (i.e., 600–800 μm). Therefore, the alternation of α overall texture is to some extent related to the β grain growth (i.e., change in β overall texture). As the reheating profile is similar for all the phase transformation routes, the main change in the α overall texture can be mostly related to the variant selection mechanism on cooling.

The variant selection is largely related to the nucleation barrier energy (ΔG^*) associated with each variant [15,23,60,61], leading to the formation of energetically favoured α variant/s. The crystallographic characteristics between the β - β grain boundaries dictate the α variant formed during the phase transformation, which has the lowest ΔG^* . For specific crystallographic orientations between adjacent β grains, the minimum ΔG^* is obtained through different means, namely a rotation of 10.5° about a $\langle 110 \rangle$ axis or a twin relationship between two adjacent β grains [16,25], a maximum deviation angle (i.e., $< 15^\circ$) of the α -variant from the adjacent β grains [17,22], low energy α/β facets/interphases [15,16], and elastic strain energy [22]. In these crystallographic conditions, similarly oriented α variants (i.e., known as grain boundary α) at either side of a prior β -grain boundary are formed, meaning that the Burgers orientation relationship can be maintained between two adjacent β -grains [15–17,22,25].

In the current experiment, intense grain growth is expected during the reheating, which affects the high temperature β -grain boundary texture, leading to the termination of boundaries at low energy plane/s (i.e., the interfacial energy between two adjacent β -grains, $\gamma_{\beta-\beta}$) [22,57,59], such as $\{1\ 1\ 0\}$ [22], and increasing the population of low angle and $\Sigma 3$ (i.e., $60^\circ/[1\ 1\ 1]$) boundaries [59]. Therefore, variant selection through the formation of grain boundary α can be enhanced for all transformation mechanisms, as it can be observed in Figs. 14a–c. Interestingly, the grain boundary α variant orientation in the $(0\ 0\ 0\ 1)$ pole figure corresponds well with the $(0\ 0\ 0\ 1)$ pole figures depicted for different phase transformations in Fig. 4, mostly located along ND-TD plane (i.e., perpendicular to ED). This suggests that the grain boundary α orientation predominantly follows the initial (recrystallized) texture components (i.e., texture memory).

Although, grain boundary α is present in all transformed microstructures, the extent of its formation changes with the phase transformation route (i.e., cooling rate), resulting in different phase transformation texture development (Fig. 14 and Fig. 4). With an increase in the cooling rate, the start and finish temperatures of the phase transformation are decreased, leading to a higher $\beta \rightarrow \alpha$ phase transformation driving force and greater β phase strength [62]. The former promotes the nucleation of a number of possible variants on a given prior β boundary due to the reduction in the difference between the nucleation driving force among different theoretical α variants (i.e., variant multiplication). This can be clearly observed in Fig. 14 where the number of α variants formed on prior β grain boundaries increases with the cooling rate. Moreover, an increase in the β phase strength with the cooling rate enhances the self-accommodation of elastic strain between α variants, ultimately restricting their growth [62–65] (i.e., microstructure refinement). As a result, the grain boundary α variant volume fraction reduces with an increase in the cooling rate, resulting in the weakening of $(0\ 0\ 0\ 1)$ texture from 14.6 MRD to 5 MRD for the coarse α microstructure (i.e., slow cooling) and martensite (i.e., water-quenching), respectively. It should be also mentioned that an increase in the cooling

rate also limits the growth of grain boundary α formed at special β grain boundaries, further weakening the $(0\ 0\ 0\ 1)$ pole figure texture intensity.

Beside the microstructure refinement, the cooling rate appears to promote specific variant arrangements in the microstructure. The nucleation of variants during the $\beta \rightarrow \alpha$ phase transformation provides a large elastic strain, which can be largely relaxed in the high transformation temperature regime (i.e. slow cooling). However, the elastic strain is minimised by different mechanisms when the transformation takes place at lower temperature (i.e., water-quenching/martensitic transformation). It is well demonstrated that the overall elastic strain associated with the phase transformation is reduced through specific variant arrangement/s [20,66,67]. Interestingly, three-variant clustering is frequently observed in the martensitic microstructure (Fig. 5), which is known to self-accommodate the shear strain associated with the martensitic transformation [20,68]. In general, the cooling rate changes the dominant variant selection mechanism from grain boundary α formation at slow cooling (i.e., coarse grained α microstructure) towards three-variant clustering at high cooling rate (i.e., martensitic structure), which results in a distinct difference in the microstructure arrangement and α overall texture.

4.2. Characterization of Intervariant Boundaries

4.2.1. Intervariant Boundary Distribution and Variant Selection

As discussed above, the change in the transformation driving force alters the variant selection mechanism, which leads to either variant multiplication (i.e., the formation of up to 12 variants; martensitic transformation), or a limited number of variants (i.e., coarse-grain microstructure) from a given β grain. In the martensitic transformation, variant multiplication can increase the variety of α variant intersections and thus, the distribution of intervariant boundaries may follow the theoretical distribution. On the contrary, limited variant formation during slow cooling condition is expected to restrict the possible variant intersections (i.e., intervariant boundaries), enhancing the populations of specific intervariant boundary/ies [20]. Interestingly, the current observation is, to some extent, different from what is expected from the extent of variant multiplication taking place at different cooling rates. Despite significant variant multiplication through the martensitic transformation, the intervariant boundary distribution differed from the theoretical distribution, showing strong maxima at a misorientation of $60^\circ/[1\ 1\ \bar{2}\ 0]$ (Fig. 9). Interestingly, it appeared that the deviation from the theoretical distribution is reduced with a decrease in the cooling rate (i.e., towards slow cooling, Table 4). This can be explained by the influence of the variant selection mechanism on the local arrangements of α variants that results from different $\beta \rightarrow \alpha$ phase transformation mechanisms.

The dominant variant selection mechanism for the slow cooling regime is identified as the formation of grain boundary α at the vicinity of special β grain boundaries. The selection of variants for the grain boundary α depends on the crystallographic characteristics of the β grain boundaries; including the interfacial energies [17,22,23,60,69] and the elastic strain energy of the transformation [20,26,33,70,71]. The elastic strain energy is largely relaxed if the transformation takes place in the high temperature regime (e.g., coarse-grain microstructure). Moreover, because of the interfacial energy constraint, only certain α orientations will form at a specific grain boundary [22]. Indeed, the nucleation of the energetically favoured grain boundary α variant can differ from one prior β grain boundary to another. Therefore, no specific variant arrangement is preferred when the grain boundary α is the dominant variant selection mechanism (i.e., the coarse-grain microstructure). In other words, a specific intervariant

Table 3
The dominant intervariant boundary planes and their characteristics.

Intervariant boundary (angle/axis)	Coarse-grain microstructure		Widmanstätten microstructure		Martensite microstructure	
	Dominant plane	Character	Dominant plane	Character	Dominant plane	Character
10.53°/[0001] 60°/[1120]	{9 1 10 0} and {7 3 4 0} Spread between (1 1 0 0) and (0 0 0 1) (4 3 1 0)	Tilt/twist Tilt	(9 1 10 0) and {7 3 4 0} Spread between (1 1 0 0)-(0 0 0 1) (4 3 1 0)	Tilt/twist Tilt	— (1 1 0 1)	— Symmetric tilt-twist
60.83°/[1.377 1 2.377 0.359]	(4 3 1 0)	9° away from (5 3 2 0) tilt boundary Twist Mixed	(4 3 1 0)	9° away from (5 3 2 0) tilt boundary	(4 3 1 0)	9° away from (5 3 2 0) tilt boundary Twist Quasi symmetric twist
63.26°/[10 5 5 3] 90°/[1 2.38 1.38 0]	(3 2 1 0) Spread between (3 2 1 0) and (1 2 1 3)	Twist Mixed	(3 2 1 0) (3 2 1 0) and (1 2 1 3)	Twist 6° and 10° away from (7 4 3 0) and (1 2 1 2) tilt respectively	(3 2 1 0) (1 1 0 1)	Twist Quasi symmetric twist

boundary may be prominent in one prior β grain boundary, but a similar arrangement is not necessarily followed in other prior β grains.

With an increase in the cooling rate, the phase transformation mostly takes place in the low temperature regime (e.g., martensitic transformation) in the pure Ti. Besides the variant multiplication, the high cooling rate alters the variant selection mechanism from grain boundary α formation towards the three-variant clustering to accommodate the transformation strain (Figs. 5-7). The intersection of variants in a given cluster crystallographically leads to a specific intervariant boundary, having a misorientation of $60^\circ/[1\ 1\ \bar{2}\ 0]$ (Fig. 5). Therefore, the presence of significantly populated $60^\circ/[1\ 1\ \bar{2}\ 0]$ intervariant in the martensite intervariant boundary distribution suggests that the three-variant formation overshadows the possible randomisation of intervariant boundary distribution due to variant multiplication. Indeed, the other intervariant boundaries associated with the Burgers OR resulted from the intersection of two distinct three-variant clusters in the martensitic microstructure. In the case of the Widmanstätten microstructure, the observed cluster population is very low (Fig. 6d) as most of the elastic transformation strain can be accommodated at the relatively higher temperature. Accordingly, the intervariant boundary distribution leans towards the theoretical distribution even though having a considerable deviation (Fig. 9 and Table 4).

4.2.2. Intervariant Boundary Plane Distribution

The intervariant boundary plane distribution is anisotropic for all microstructures formed through different transformation paths (Fig. 10 and Table 3). However, the distribution is relatively different for each transformation mechanism. In general, the grain boundary network (i.e., population and/or plane orientation) is largely influenced by alloy composition [40,41], texture [72-75], interfacial energy [72,76-78] and phase transformation mechanism [46]. The role of alloying elements on grain boundary characteristics can be ruled out here as the same alloy (commercially pure titanium) was used throughout the study. Moreover, the change in the overall texture characteristics mostly affects the boundary population rather than the grain boundary plane orientation [46]. This is consistent with the current result, where the boundary plane orientations are largely similar for all phase transformation routes (Fig. 12). However, it is anticipated through both simulations [72,73,79] and experimental studies [31,34,79,80] that the boundaries having high populations lie with the planes with the least energy. For the current study, an estimation of a relative interface/boundary energy was obtained from the interplanar spacing of the related boundary planes [81], assuming a large interplanar spacing represents an interface with better fit and a correspondingly low surface energy, and that the opposite is true for small interplanar spacings. Accordingly, the interplanar spacing values calculated for the boundary planes identified in the stereological projections in Fig. 10 are summarised in Table 5. The interplanar spacing are 2.0284, 1.8019, 1.7038 and 1.4755 Å for the (0 0 0 1), (1 0 $\bar{1}$ 1), (1 0 $\bar{1}$ 0) and (1 1 $\bar{2}$ 0) planes, respectively. Therefore, the lowest energy is attributed to the (0 0 0 1) boundary plane, though it appears to have the lowest population in all transformation paths (Fig. 10). Assuming the interplanar spacings are correlated to relative energies, then we must conclude that in these cases, the energy does not have a strong effect on the distribution of grain boundary planes.

The intersections of two distinct variants associated with the Burgers OR are schematically presented in Fig. 15, which corresponds with the intervariant plane distributions measured experimentally for the intervariant boundaries formed during the different phase transformation paths (Fig. 12). It appears that the crystallography of the phase transformation path potentially dictates the termination of intervariant boundary planes on prismatic, pyramidal, near prismatic/pyramidal and/or basal orientations. The latter is likely to be observed for the $10^\circ/[0\ 0\ 0\ 1]$ intervariant boundary. However, the distribution of $10^\circ/[0\ 0\ 0\ 1]$ intervariant boundary displays a minimum at the (0 0 0 1) orientation (Figs. 10a-c), suggesting that it tends to terminate on

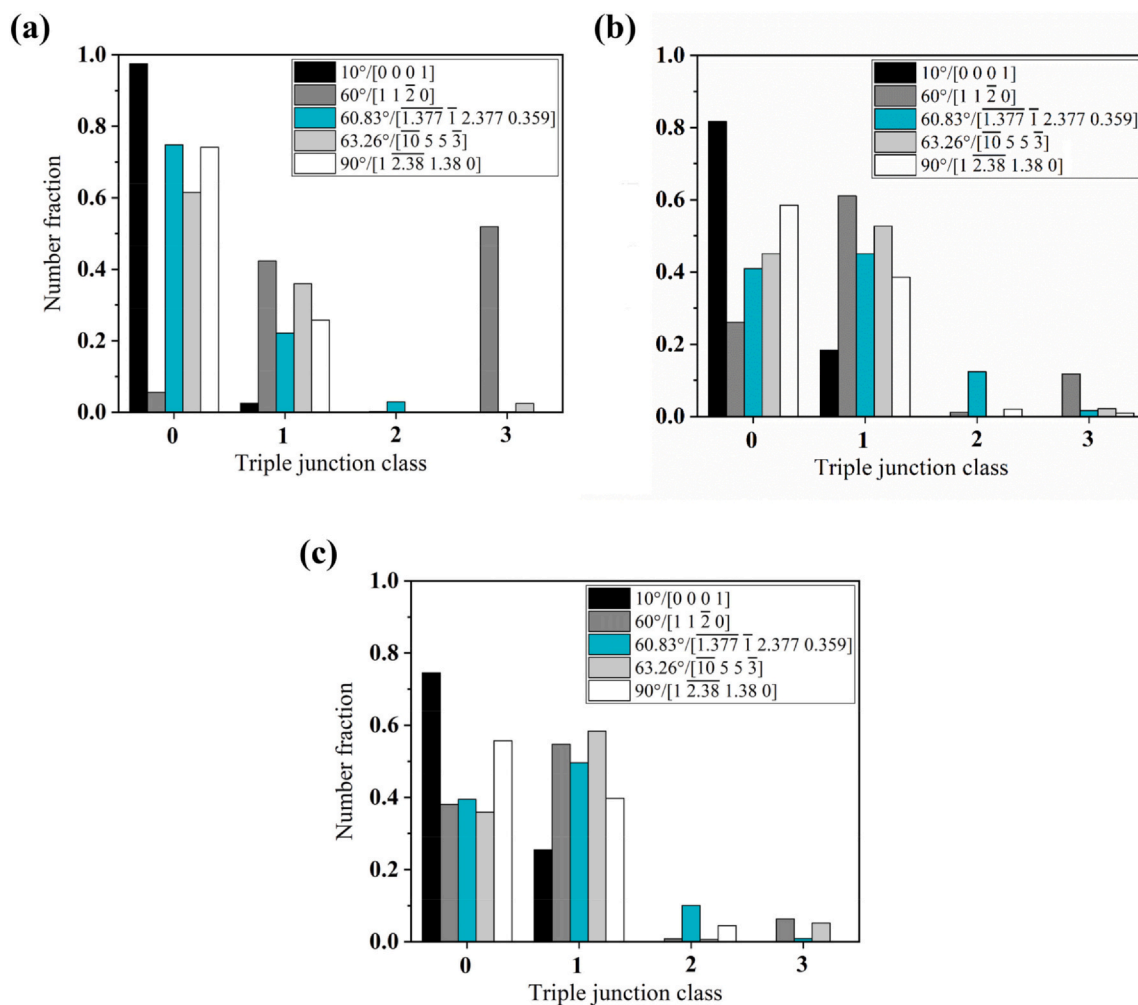


Fig. 13. Fraction of specific types of intervariant boundaries present in different types of triple junctions for (a) martensite, Widmanstätten and (c) coarse-grain microstructures. Triple junction classes of 0 through 3 represent the number of a given intervariant boundary present at the triple junction, as shown schematically in Fig. 3.

the prismatic planes rather than the basal planes for all phase transformation mechanisms. This can be a result of phase transformation crystallographic constraints rather than low energy interfaces, as (0 0 0 1) plane orientation is expected to have the minimum energy based on the interplanar spacing calculation (Table 5). It is worth mentioning that the population of this plane is also minimum among the different intervariant boundaries associated with the Burgers OR for all phase transformation routes (i.e., < 10%, Fig. 9). Therefore, the basal plane is expected to have a minimal influence on the overall boundary plane distribution (Fig. 10).

The most obvious effect of the phase transformation route on the grain boundary plane distribution is the presence of strong peak at the {1 0 1} pyramidal orientation for the martensitic structure, which is absent for both Widmanstätten and coarse-grain microstructures (Fig. 12). This results from the preference for the triangular variant selection arrangement in the martensitic transformation, which significantly increases the population of intervariant boundaries with the 60°/[1 1 2̄ 0] misorientation (Fig. 9) and (1̄ 1 0 1) boundary plane orientations (Fig. 11d). Interestingly, this plane orientation was shown, using a molecular dynamics calculation, to have a minimum energy arrangement [82]. In other words, the local variant selection in the martensitic transformation leads to the formation boundaries with the minimum energy to accommodate the strain associated with the martensitic transformation. In general, the phase transformation strongly dictates the grain boundary network characteristics (i.e., population

and plane orientation) through the Burgers OR crystallography and the variant selection mechanism, which may not necessarily result the intervariant boundary plane/s with the minimum energy configuration.

4.3. Connectivity of the Grain Boundary Network

The boundary triple junction analysis reveals a significant change in the grain boundary network that depends on the phase transformation mechanism (Fig. 13). Class 3 triple junctions, with three 60°/[1 1 2̄ 0] intervariant boundaries appear in triple junction class 3 in the martensite. This suggests that the grain boundary network is largely connected by the 60°/[1 1 2̄ 0] intervariant boundaries. However, the class 3 triple junction frequency significantly reduces with a slower cooling rates to ~5% and 3% for the Widmanstätten and coarse-grain microstructures, respectively. This is consistent with the triangular morphology, which is frequently observed in the martensitic microstructure (Fig. 5) and also demonstrated through the phenomenological theory [48]. Based on the fact that the 60°/[1 1 2̄ 0] intervariant is mostly terminated at the pyramidal (1 0 1) planes, it can be concluded that the martensite transformation results into a more connected network of this type of intervariant boundary in comparison with the Widmanstätten and coarse-grain microstructures. With a decrease in the cooling rate, most types of intervariant boundaries appear with a similar frequency in class 3 triple junctions. This suggests that the slow cooling rate promotes the randomly connected intervariant boundaries at the triple

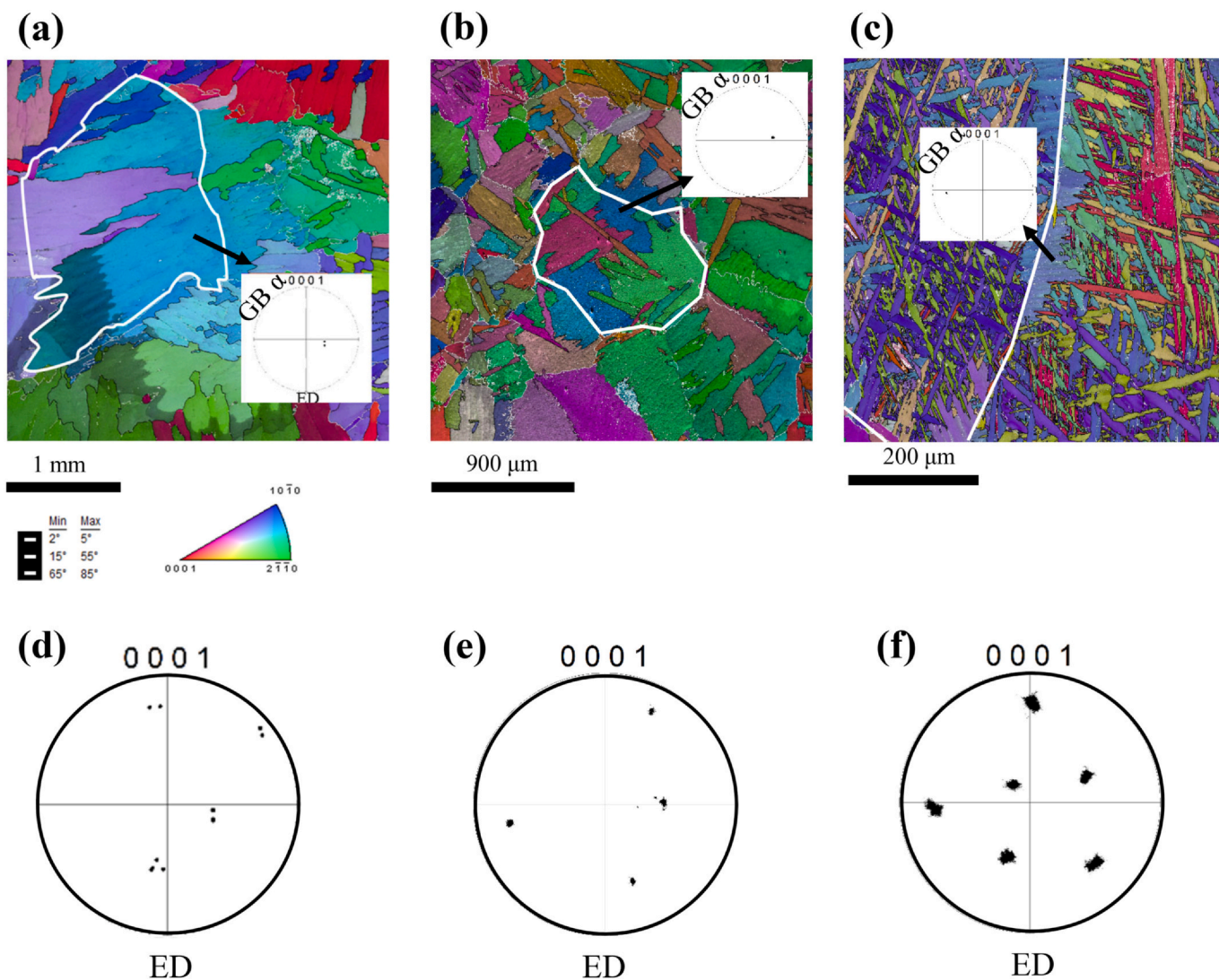


Fig. 14. The image quality map and imposed grain boundary map of (a) diffusional, (b) diffusional-assisted and (c) martensitic microstructures. The (0001) pole figures of variants formed in a prior beta grain (the highlighted region) corresponding to (d) diffusional, (e) diffusion-assisted and (f) martensite transformation.

Table 4

Calculated absolute deviation percentage (i.e., Δ) of intervariant boundary population from the possible random intersection of α -variants during different transformation path naming diffusional, diffusional-assisted and martensitic transformation.

Transformation path Intervariant boundary	Diffusional	Diffusional-assisted	Martensite
10.53°/[0001]	$\Delta = 0.4\%$	$\Delta = 1.77\%$	$\Delta = 7.5\%$
60°/[11 $\bar{2}$ 0]	$\Delta = 2.83\%$	$\Delta = 3.2\%$	$\Delta = 40.7\%$
60.83°/[1.377 $\bar{1}$ 2.377 0.359]	$\Delta = 3.07\%$	$\Delta = 6.73\%$	$\Delta = 24.86\%$
63.26°/[$\bar{1}$ 0 5 5 $\bar{3}$]	$\Delta = 1.68\%$	$\Delta = 2.87\%$	$\Delta = 4.78\%$
90°/[1 $\bar{2}$.38 1.38 0]	$\Delta = 1.38\%$	$\Delta = 3.18\%$	$\Delta = 13.18\%$

junctions.

5. Conclusion

In the current study, the influence of the phase transformation mechanism on the grain boundary network characteristics was investigated in a commercially pure Ti through a five-parameter analysis of the boundary character distribution and an analysis of the triple junctions. The followings are the notable findings on this investigation:

Table 5

The interplanar spacing (d_{kl}) for different measured intervariant planes and their corresponding population.

Intervariant boundary	Plane	Interplanar spacing (Å)
Fig. 10 All boundaries	(1 0 $\bar{1}$ 0)	0.8519 or 1.7038 ^a
	(1 1 $\bar{2}$ 0)	1.4755
	(0 0 0 1)	2.0284
	(1 0 $\bar{1}$ 1)	0.3604 or 1.8019 ^a
Fig. 12 60°/[1 1 $\bar{2}$ 0] 60.83°/[1.377 $\bar{1}$ 2.377 0.359] 63.26°/[$\bar{1}$ 0 5 5 $\bar{3}$] 90°/[1 $\bar{2}$.38 1.38 0]	(4 $\bar{1}$ $\bar{3}$ 0)	0.2363 or 0.4725 ^a
	($\bar{1}$ 1 0 1)	0.3604 or 1.8019 ^a
	($\bar{4}$ 3 1 0)	0.2363 or 0.4725 ^a
	(5 3 2 0)	0.1954 or 0.3908 ^a
	($\bar{4}$ 3 1 1)	0.1164 or 0.5819 ^a
	(1 $\bar{1}$ 0 1)	0.3604 or 1.8019 ^a
	(3 $\bar{2}$ $\bar{1}$ 0)	0.3219 or 0.6439 ^a
	(1 $\bar{1}$ 0 1)	0.1662 or 0.8308 ^a

^a Taking into account the structure factor as the plane passing through an additional atom [81].

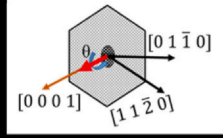
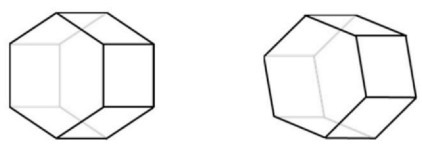
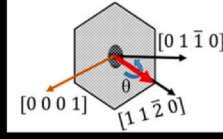
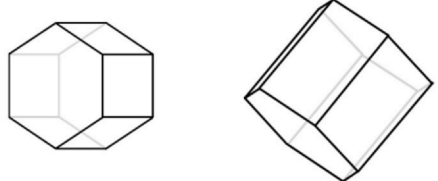
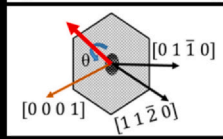
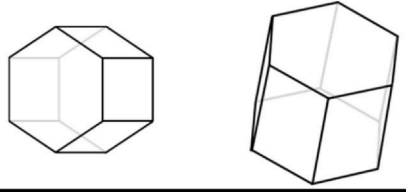
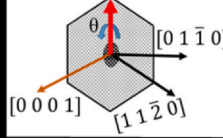
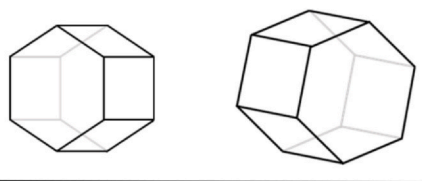
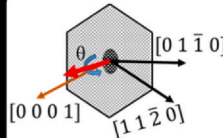
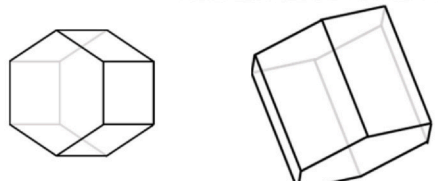
Intervariant boundary	Crystallographic depiction	Possible crystallographic plane intersection
$10.53^\circ/[0\ 0\ 0\ 1]$ 		Basal-basal Prismatic-prismatic
$60^\circ/[1\ 1\ \bar{2}\ 0]$ 		Prism-Prism Pyramidal-Prism Pyramidal-Pyramidal
$60.83^\circ/$ $[\bar{1}.377\ \bar{1}\ 2.377\ 0.359]$ 		Basal-Prism Pyramidal-Basal Pyramidal-Pyramidal
$63.26^\circ/[\bar{1}0\ 5\ 5\ \bar{3}]$ 		Basal-Prism Pyramidal-Basal Pyramidal-Pyramidal
$90^\circ/[1\ \bar{2}.38\ 1.38\ 0]$ 		Basal-Prism Pyramidal-Basal

Fig. 15. The crystallographic orientations of two different α -variants and the corresponding crystallographic plane orientation.

- 1) The texture of the commercially pure titanium subjected to different phase transformation mechanisms was qualitatively similar to the as-received material. However, the overall transformation texture changed with the transformation route. Variant multiplication in the martensitic transformation decreased the strength of the texture while the nucleation and growth of variants selected through special prior β grain boundaries in the more slowly cooled samples strengthened the overall texture.
- 2) Despite significant variant multiplication through the martensitic transformation, the interviant boundary population in the martensite was governed by the local variant selection mechanism influenced by the transformation strain (i.e., three variant clustering). This led to a significant population of twin related $60^\circ/[1\ 1\ \bar{2}\ 0]$ interviant boundaries. On the other hand, the Widmanstätten and coarse-grain structures had no specific variant arrangement resulting from a decrease in the role of transformation strain, leading to a more nearly random distribution of interviant boundaries.
- 3) The interviant boundary plane distribution was anisotropic for all the microstructures. It was demonstrated that the boundary planes were mostly terminated on high energy prismatic $\{hki0\}$ orientations for all transformation paths. However, the martensitic transformation showed an extra tendency for pyramidal $(\bar{1}\ 1\ 0\ 1)$ planes, which were associated with the highly populated symmetric tilt $60^\circ/[1\ 1\ \bar{2}\ 0]$ interviant boundaries.
- 4) The change in the phase transformation greatly influenced the connectivity of the interviant boundaries in the corresponding microstructure. It was shown that the local variant selection mechanism significantly enhanced the connectivity of the $60^\circ/[1\ 1\ \bar{2}\ 0]$ interviant boundaries in the martensite. With a decrease in the cooling rate, the connectivity of interviant boundaries was significantly reduced.

Declaration of Competing Interest

The authors declare that they have no known competing financial interests or personal relationships that could have appeared to influence the work reported in this paper.

Acknowledgements

Extensive discussions with Prof. Bevis Hutchinson are greatly acknowledged. Deakin University's Advanced Characterization Facility is acknowledged for use of the EBSD instruments and assistance from Dr. Mark Nave.

References

- [1] S. Banerjee, P. Mukhopadhyay, Acknowledgements, Phase Transform. Examples

- from Titan. Zircon. Alloy, 2007, [https://doi.org/10.1016/S1470-1804\(07\)80053-8](https://doi.org/10.1016/S1470-1804(07)80053-8).
- [2] G. Lütjering, J.C. Williams, Titanium, Second ed., Springer-Verlag, Berlin Heidelberg, 2007, <https://doi.org/10.1007/978-3-540-73036-1>.
- [3] I. Lonardelli, N. Gey, H.R. Wenk, M. Humbert, S.C. Vogel, L. Lutterotti, In situ observation of texture evolution during $\alpha \rightarrow \beta$ and $\beta \rightarrow \alpha$ phase transformations in titanium alloys investigated by neutron diffraction, *Acta Mater.* 55 (2007) 5718–5727, <https://doi.org/10.1016/j.actamat.2007.06.017>.
- [4] M.R. Daymond, R.A. Holt, S. Cai, P. Mosbrucker, S.C. Vogel, Texture inheritance and variant selection through an hcp-bcc-hcp phase transformation, *Acta Mater.* 58 (2010) 4053–4066, <https://doi.org/10.1016/j.actamat.2010.03.012>.
- [5] N. Gey, M. Humbert, H. Moustahfid, Study of the $\alpha \rightarrow \beta$ phase transformation of a Ti-6Al-4V sheet by means of texture change, *Scr. Mater.* 42 (2000) 525–530, [https://doi.org/10.1016/S1359-6462\(99\)00396-6](https://doi.org/10.1016/S1359-6462(99)00396-6).
- [6] W.G.G. Burgers, On the process of transition of the cubic-body-centered modification into the hexagonal-close-packed modification of zirconium, *Physica 1* (1934) 561–586, [https://doi.org/10.1016/S0031-8914\(34\)80244-3](https://doi.org/10.1016/S0031-8914(34)80244-3).
- [7] G.C. Obasi, R.J. Moat, D.G. Leo Prakash, W. Kockelmann, J. Quinta Da Fonseca, M. Preuss, In situ neutron diffraction study of texture evolution and variant selection during the $\alpha \rightarrow \beta \rightarrow \alpha$ phase transformation in Ti-6Al-4V, *Acta Mater.* 60 (2012) 7169–7182, <https://doi.org/10.1016/j.actamat.2012.09.026>.
- [8] R.J. Wilson, V. Randle, W.J. Evans, The influence of the burgers relation on crack propagation in a near α -titanium alloy, *Philos. Mag. A Phys. Condens. Matter Struct. Defects Mech. Prop.* 76 (1997) 471–480, <https://doi.org/10.1080/01418619708209986>.
- [9] M.R. Bache, Processing titanium alloys for optimum fatigue performance, *Int. J. Fatigue* 21 (1999) 105–111, [https://doi.org/10.1016/S0142-1123\(99\)00061-4](https://doi.org/10.1016/S0142-1123(99)00061-4).
- [10] A.E. Medvedev, H.P. Ng, R. Lapovok, Y. Estrin, T.C. Lowe, V.N. Anumalasetty, Effect of bulk microstructure of commercially pure titanium on surface characteristics and fatigue properties after surface modification by sand blasting and acid-etching, *J. Mech. Behav. Biomed. Mater.* 57 (2016) 55–68, <https://doi.org/10.1016/j.jmbbm.2015.11.035>.
- [11] T. Furuhashi, H. Nakamori, T. Maki, Crystallography of α phase precipitated on dislocations and deformation twin boundaries in a β titanium alloy, *Mater. Trans.* 33 (1992) 585–595, <https://doi.org/10.2320/matertrans1989.33.585>.
- [12] T. Furuhashi, T. Maki, Variant selection in heterogeneous nucleation on defects in diffusional phase transformation and precipitation, *Mater. Sci. Eng. A* 312 (2001) 145–154, [https://doi.org/10.1016/S0921-5093\(00\)01904-3](https://doi.org/10.1016/S0921-5093(00)01904-3).
- [13] S.M.C. van Bohemen, A. Kamp, R.H. Petrov, L.A.I. Kestens, J. Sietsma, Nucleation and variant selection of secondary α plates in a β Ti alloy, *Acta Mater.* 56 (2008) 5907–5914, <https://doi.org/10.1016/j.actamat.2008.08.016>.
- [14] R. Shi, Y. Zheng, D. Wang, H. Fraser, Y. Wang, I. Nucleation, N. Band, M. Field, A.I. Energy, Heterogeneous nucleation during in titanium alloys transformation, *Proc. 13th World Conf. Titan*, 1 2016, pp. 1931–1936, <https://doi.org/10.1002/9781119296126.ch323>.
- [15] T. Furuhashi, S. Takagi, H. Watanabe, T. Maki, Crystallography of grain boundary α precipitates in a β titanium alloy, *Metall. Mater. Trans. A* 27 (1996) 1635–1646, <https://doi.org/10.1007/BF02649821>.
- [16] D. Bhattacharyya, G.B. Viswanathan, R. Denkenberger, D. Furrer, H.L. Fraser, The role of crystallographic and geometrical relationships between α and β phases in an α/β titanium alloy, *Acta Mater.* 51 (2003) 4679–4691, [https://doi.org/10.1016/S1359-6454\(03\)00179-4](https://doi.org/10.1016/S1359-6454(03)00179-4).
- [17] R. Shi, V. Dixit, H.L. Fraser, Y. Wang, Variant selection of grain boundary α by special prior β grain boundaries in titanium alloys, *Acta Mater.* 75 (2014) 156–166, <https://doi.org/10.1016/j.actamat.2014.05.003>.
- [18] M. Humbert, N. Gey, Elasticity-based model of the variant selection observed in the β to α phase transformation of a Zircalloy-4 sample, *Acta Mater.* 51 (2003) 4783–4790, [https://doi.org/10.1016/S1359-6454\(03\)00318-5](https://doi.org/10.1016/S1359-6454(03)00318-5).
- [19] R. Shi, Y. Wang, Variant selection during α precipitation in Ti-6Al-4V under the influence of local stress - a simulation study, *Acta Mater.* 61 (2013) 6006–6024, <https://doi.org/10.1016/j.actamat.2013.06.042>.
- [20] S.C. Wang, M. Aindow, M.J. Starink, Effect of self-accommodation on α/α boundary populations in pure titanium, *Acta Mater.* 51 (2003) 2485–2503, [https://doi.org/10.1016/S1359-6454\(03\)00035-1](https://doi.org/10.1016/S1359-6454(03)00035-1).
- [21] D. Qiu, R. Shi, D. Zhang, W. Lu, Y. Wang, Variant selection by dislocations during α precipitation in α/β titanium alloys, *Acta Mater.* 88 (2015) 218–231, <https://doi.org/10.1016/j.actamat.2014.12.044>.
- [22] R. Shi, V. Dixit, G.B. Viswanathan, H.L. Fraser, Y. Wang, Experimental assessment of variant selection rules for grain boundary α in titanium alloys, *Acta Mater.* 102 (2016) 197–211, <https://doi.org/10.1016/j.actamat.2015.09.021>.
- [23] J.K. Lee, H.I. Aaronson, Influence of faceting upon the equilibrium shape of nuclei at grain boundaries-II. Three-dimensions, *Acta Metallurg.* 23 (1975) 809–820.
- [24] J.K. Lee, H.I. Aaronson, Influence of faceting upon the equilibrium shape of nuclei at grain boundaries—I. Two-dimensions, *Acta Metall.* 23 (1975) 799–808.
- [25] D. Bhattacharyya, G.B. Viswanathan, H.L. Fraser, Crystallographic and morphological relationships between β phase and the Widmanstätten and allotriomorphic α phase at special β grain boundaries in an α/β titanium alloy, *Acta Mater.* 55 (2007) 6765–6778, <https://doi.org/10.1016/j.actamat.2007.08.029>.
- [26] N. Stanford, P.S. Bate, Crystallographic variant selection in Ti-6Al-4V, *Acta Mater.* 52 (2004) 5215–5224, <https://doi.org/10.1016/j.actamat.2004.07.034>.
- [27] E. Lee, R. Banerjee, S. Kar, D. Bhattacharyya, H.L. Fraser, Selection of α variants during microstructural evolution in α/β titanium alloys, *Philos. Mag.* 87 (2007) 3615–3627, <https://doi.org/10.1080/14786430701373672>.
- [28] D. Banerjee, A.L. Pilchak, J.C. Williams, Processing, structure, texture and micro-texture in titanium alloys, *Mater. Sci. Forum* 710 (2012) 66–84, <https://doi.org/10.4028/www.scientific.net/MSF.710.66>.
- [29] D. Banerjee, J.C. Williams, Perspectives on titanium science and technology, *Acta Mater.* 61 (2013) 844–879, <https://doi.org/10.1016/j.actamat.2012.10.043>.
- [30] N. Stanford, P.S. Bate, The martensitic transformation texture in Ti-6Al-4V, *Mater. Sci. Forum* 495–497 (2005) 669–674, <https://doi.org/10.4028/www.scientific.net/MSF.495-497.669>.
- [31] H. Beladi, Q. Chao, G.S. Rohrer, Variant selection and intervariant crystallographic planes distribution in martensite in a Ti-6Al-4V alloy, *Acta Mater.* 80 (2014) 478–489, <https://doi.org/10.1016/j.actamat.2014.06.064>.
- [32] A.G. Khundzhua, A.G. Ptitsyn, E.A. Brovkina, S. Chzhen, Self-accommodation of crystals of martensitic phases in titanium and zirconium based alloys, *Phys. Met. Metallogr.* 113 (2012) 1035–1040, <https://doi.org/10.1134/s0031918x12110117>.
- [33] D. Srivastava, K. Madangopal, S. Banerjee, S. Ranganathan, Self accommodation morphology of martensite variants in Zr-2.5 wt % Nb alloy, *Acta Metall. Mater.* 41 (1993) 3445–3454.
- [34] G.S. Rohrer, D.M. Saylor, B. El Dasher, B.L. Adams, A.D. Rollet, P. Wynblatt, The distribution of internal interfaces in polycrystals, *Zeitschrift Für Met* 95 (2004) 197–214, <https://doi.org/10.3139/j.146.017934>.
- [35] N. Haghdadi, P. Cizek, P.D. Hodgson, V. Tari, G.S. Rohrer, H. Beladi, Effect of ferrite-to-austenite phase transformation path on the interface crystallographic character distributions in a duplex stainless steel, *Acta Mater.* 145 (2018) 196–209, <https://doi.org/10.1016/j.actamat.2017.11.057>.
- [36] A.P. Sutton, E.P. Banks, A.R. Warwick, The five-dimensional parameter space of grain boundaries, *Proc. R. Soc. A Math. Phys. Eng. Sci.* 471 (2015) 20150442, <https://doi.org/10.1098/rspa.2015.0442>.
- [37] I. Ghamarian, P. Samimi, G.S. Rohrer, P.C. Collins, Determination of the five parameter grain boundary character distribution of nanocrystalline alpha-zirconium thin films using transmission electron microscopy, *Acta Mater.* 130 (2017) 164–176, <https://doi.org/10.1016/j.actamat.2017.03.041>.
- [38] H. Beladi, G.S. Rohrer, A.D. Rollet, V. Tari, P.D. Hodgson, The distribution of intervariant crystallographic planes in a lath martensite using five macroscopic parameters, *Acta Mater.* 63 (2014) 86–98, <https://doi.org/10.1016/j.actamat.2013.10.010>.
- [39] M.N. Kelly, K. Glowinski, N.T. Nuhfer, G.S. Rohrer, The five parameter grain boundary character distribution of α -Ti determined from three-dimensional orientation data, *Acta Mater.* 111 (2016) 22–30, <https://doi.org/10.1016/j.actamat.2016.03.029>.
- [40] M. Baram, D. Chatain, W.D. Kaplan, Nanometer-thick equilibrium films: the interface between thermodynamics and atomistics, *Science* 80 (332) (2011) 206–209, <https://doi.org/10.1126/science.1201596>.
- [41] S.J. Dillon, M. Tang, W.C. Carter, M.P. Harmer, Complexion: a new concept for kinetic engineering in materials science, *Acta Mater.* 55 (2007) 6208–6218, <https://doi.org/10.1016/j.actamat.2007.07.029>.
- [42] H. Beladi, N.T. Nuhfer, G.S. Rohrer, The five-parameter grain boundary character and energy distributions of a fully austenitic high-manganese steel using three dimensional data, *Acta Mater.* 70 (2014) 281–289, <https://doi.org/10.1016/j.actamat.2014.02.038>.
- [43] H. Beladi, G.S. Rohrer, The relative grain boundary area and energy distributions in a ferritic steel determined from three-dimensional electron backscatter diffraction maps, *Acta Mater.* 61 (2013) 1404–1412, <https://doi.org/10.1016/j.actamat.2012.11.017>.
- [44] N. Haghdadi, P. Cizek, P.D. Hodgson, Y. He, B. Sun, J.J. Jonas, G.S. Rohrer, H. Beladi, New insights into the interface characteristics of a duplex stainless steel subjected to accelerated ferrite-to-austenite transformation, *J. Mater. Res.* 55 (2020) 5322–5339, <https://doi.org/10.1007/s10853-020-04358-3>.
- [45] N. Haghdadi, A. Zarei-Hanzaki, E. Farabi, P. Cizek, H. Beladi, P.D. Hodgson, Strain rate dependence of ferrite dynamic restoration mechanism in a duplex low-density steel, *Mater. Des.* 132 (2017), <https://doi.org/10.1016/j.matdes.2017.07.009>.
- [46] H. Beladi, G.S. Rohrer, The role of thermomechanical routes on the distribution of grain boundary and interface plane orientations in transformed microstructures, *Metall. Mater. Trans. A* 48 (2017) 2781–2790, <https://doi.org/10.1007/s11661-016-3630-4>.
- [47] V. Randle, G.S. Rohrer, Y. Hu, Five-parameter grain boundary analysis of a titanium alloy before and after low-temperature annealing, *Scr. Mater.* 58 (2008) 183–186, <https://doi.org/10.1016/j.scriptamat.2007.09.044>.
- [48] E. Farabi, P.D. Hodgson, G.S. Rohrer, H. Beladi, Five-parameter intervariant boundary characterization of martensite in commercially pure titanium, *Acta Mater.* 154 (2018) 147–160, <https://doi.org/10.1016/j.actamat.2018.05.023>.
- [49] Servotestsystems, TMTS-Thermo-Mechanical Treatment Simulator, <http://www.servotestsystems.com/high-rate-systems/tmts-thermo-mechanical-treatment-simulator.html>, (2020).
- [50] D.M. Saylor, B. El Dasher, Y. Pang, H.M. Miller, P. Wynblatt, A.D. Rollet, G.S. Rohrer, Habits of grains in dense polycrystalline solids, *J. Am. Ceram. Soc.* 87 (2004) 724–726, <https://doi.org/10.1111/j.1551-2916.2004.00724.x>.
- [51] E. Farabi, V. Tari, P.D. Hodgson, G.S. Rohrer, H. Beladi, On the grain boundary network characteristics in a martensitic Ti-6Al-4V alloy, *J. Mater. Sci.* 55 (November) (2020) 15299–15321, <https://doi.org/10.1007/s10853-020-05075-7>.
- [52] Z. Zeng, Y. Zhang, S. Jonsson, Deformation behaviour of commercially pure titanium during simple hot compression, *Mater. Des.* 30 (2009) 3105–3111, <https://doi.org/10.1016/j.matdes.2008.12.002>.
- [53] N. Gey, M. Humbert, Characterization of the variant selection occurring during the α to β phase transformations of a cold rolled titanium sheet, *Acta Mater.* 50 (2002) 277–287, [https://doi.org/10.1016/S1359-6454\(01\)00351-2](https://doi.org/10.1016/S1359-6454(01)00351-2).
- [54] K. Glowinski, A. Morawiec, A toolbox for geometric grain boundary characterization, *Proc. 1st Int. Conf. 3D Mater. Sci. Springer, Cham*, 2012, pp. 119–124.
- [55] C. Jourdan, J. Gastaldi, P. Marzo, G. Grange, In situ statistical study of the nucleation, the variant selection and the orientation memory effect during the $\alpha \rightarrow \beta$ titanium martensitic transformation, *J. Mater. Sci.* 26 (1991) 4355–4360, <https://doi.org/10.1016/j.actamat.2012.10.043>.

- doi.org/10.1007/BF00543651.
- [56] J. Romero, M. Preuss, J. Quinta da Fonseca, Texture memory and variant selection during phase transformation of a zirconium alloy, *Acta Mater.* 57 (2009) 5501–5511, <https://doi.org/10.1016/j.actamat.2009.07.046>.
- [57] G.C. Obasi, S. Biroscas, J. Quinta Da Fonseca, M. Preuss, Effect of β grain growth on variant selection and texture memory effect during $\alpha \rightarrow \beta \rightarrow \alpha$ phase transformation in Ti-6 Al-4 v, *Acta Mater.* 60 (2012) 1048–1058, <https://doi.org/10.1016/j.actamat.2011.10.038>.
- [58] N. Bozzolo, N. Dewobroto, T. Grosdidier, F. Wagner, Texture evolution during grain growth in recrystallized commercially pure titanium, *Mater. Sci. Eng. A* 397 (2005) 346–355, <https://doi.org/10.1016/j.msea.2005.02.049>.
- [59] G.C. Obasi, J.Q. da Fonseca, D. Rugg, M. Preuss, The effect of β grain coarsening on variant selection and texture evolution in a near- β Ti alloy, *Mater. Sci. Eng. A* 576 (2013) 272–279, <https://doi.org/10.1016/j.msea.2013.04.018>.
- [60] J.K. Lee, H.I. Aaronson, Influence of faceting upon the equilibrium shape of nuclei at grain boundaries-I. Two-dimensions, *Acta Metall.* 23 (1975) 799–808, [https://doi.org/10.1016/0001-6160\(75\)90197-2](https://doi.org/10.1016/0001-6160(75)90197-2).
- [61] H.I. Aaronson, G. Spanos, R.A. Masamura, R.G. Vardiman, D.W. Moon, E.S.K. Menon, M.G. Hall, Sympathetic nucleation: an overview, *Mater. Sci. Eng. B* 32 (1995) 107–123, [https://doi.org/10.1016/0921-5107\(95\)80022-0](https://doi.org/10.1016/0921-5107(95)80022-0).
- [62] H. Beladi, V. Tari, I.B. Timokhina, P. Cizek, G.S. Rohrer, A.D. Rollett, P.D. Hodgson, On the crystallographic characteristics of nanobainitic steel, *Acta Mater.* 127 (2017) 426–437, <https://doi.org/10.1016/j.actamat.2017.01.058>.
- [63] T. Furuahara, H. Kawata, S. Morito, T. Maki, Crystallography of upper bainite in Fe-Ni-C alloys, *Mater. Sci. Eng. A* 431 (2006) 228–236, <https://doi.org/10.1016/j.msea.2006.06.032>.
- [64] H. Beladi, Y. Adachi, I. Timokhina, P.D. Hodgson, Crystallographic analysis of nanobainitic steels, *Scr. Mater.* 60 (2009) 455–458, <https://doi.org/10.1016/j.scriptamat.2008.11.030>.
- [65] N. Takayama, G. Miyamoto, T. Furuahara, Effects of transformation temperature on variant pairing of bainitic ferrite in low carbon steel, *Acta Mater.* 60 (2012) 2387–2396, <https://doi.org/10.1016/j.actamat.2011.12.018>.
- [66] H.K.D.H. Bhadeshia, H. Abreu, S. Kundu, Calculation of crystallography texture due to displacive transformations, *Int. J. Mater. Res.* 99 (2008) 342–346, <https://doi.org/10.3139/146.101645>.
- [67] H. Bhadeshia, S. Kundu, Mathematics of crystallographic texture in martensitic and related transformations, *Microstruct. Texture Steels* (2009) 19–31, https://doi.org/10.1007/978-1-84882-454-6_2.
- [68] S. Balachandran, A. Kashiwar, A. Choudhury, D. Banerjee, R. Shi, Y. Wang, On variant distribution and coarsening behavior of the α phase in a metastable β titanium alloy, *Acta Mater.* 106 (2016) 374–387, <https://doi.org/10.1016/j.actamat.2016.01.023>.
- [69] R. Shi, N. Ma, Y. Wang, Predicting equilibrium shape of precipitates as function of coherency state, *Acta Mater.* 60 (2012) 4172–4184, <https://doi.org/10.1016/j.actamat.2012.04.019>.
- [70] G. Reisner, F. Fischer, Y. Wen, E. Werner, Interaction energy between martensitic variants, *Met. Mater.* 30 (1999) 2583–2590, <https://doi.org/10.1007/s11661-999-0297-0>.
- [71] D. Srivastava, S. Banerjee, S. Ranganathan, The crystallography of the BCC to HCP (orthohexagonal) martensitic transformation in dilute Zr-Nb alloys: part I: lattice strain and lattice invariant shear, *Trans. Indian Inst. Metals* 57 (2004) 205–223, <http://www.igcar.gov.in/transiim/2004/TP-1887.pdf>.
- [72] J. Gruber, D.C. George, A.P. Kuprat, G.S. Rohrer, A.D. Rollett, Effect of anisotropic grain boundary properties on grain boundary plane distributions during grain growth, *Scr. Mater.* 53 (2005) 351–355, <https://doi.org/10.1016/j.scriptamat.2005.04.004>.
- [73] J. Gruber, H.M. Miller, T.D. Hoffmann, G.S. Rohrer, A.D. Rollett, Misorientation texture development during grain growth. Part I: simulation and experiment, *Acta Mater.* 57 (2009) 6102–6112, <https://doi.org/10.1016/j.actamat.2009.08.036>.
- [74] W. Wang, Y. Lin, P. Dai, G.S. Rohrer, W. Zhang, Grain boundary plane distributions in a cold rolled and annealed high purity iron, *Mater. Charact.* 122 (2016) 6–13, <https://doi.org/10.1016/j.matchar.2016.10.021>.
- [75] H. Beladi, P. Cizek, A.S. Taylor, G.S. Rohrer, P.D. Hodgson, Static softening in a Ni-30Fe austenitic model alloy after hot deformation: microstructure and texture evolution, *Metall. Mater. Trans. A Phys. Metall. Mater. Sci.* 48 (2017) 855–867, <https://doi.org/10.1007/s11661-016-3880-1>.
- [76] A.D. Rollett, Crystallographic texture change during grain growth, *Jom* 56 (2004) 63–68, <https://doi.org/10.1007/s11837-004-0075-9>.
- [77] S.J. Dillon, G.S. Rohrer, Mechanism for the development of anisotropic grain boundary character distributions during normal grain growth, *Acta Mater.* 57 (2009) 1–7, <https://doi.org/10.1016/j.actamat.2008.08.062>.
- [78] D.M. Saylor, A. Morawiec, G.S. Rohrer, The relative free energies of grain boundaries in magnesia as a function of five macroscopic parameters, *Acta Mater.* 51 (2003) 3675–3686, [https://doi.org/10.1016/S1359-6454\(03\)00182-4](https://doi.org/10.1016/S1359-6454(03)00182-4).
- [79] S. Ratanaphan, D.L. Olmsted, V.V. Bulatov, E.A. Holm, A.D. Rollett, G.S. Rohrer, Grain boundary energies in body-centered cubic metals, *Acta Mater.* 88 (2015) 346–354, <https://doi.org/10.1016/j.actamat.2015.01.069>.
- [80] G.S. Rohrer, J. Li, S. Lee, A.D. Rollett, M. Groeber, M.D. Uchic, Deriving grain boundary character distributions and relative grain boundary energies from three-dimensional EBSD data, *Mater. Sci. Technol.* 26 (2010) 661–669, <https://doi.org/10.1179/026708309X12468927349370>.
- [81] Q. Fan, A new method of calculating interplanar spacing: the position-factor method, *J. Appl. Crystallogr.* 45 (2012) 1303–1308, <https://doi.org/10.1107/S0021889812037764>.
- [82] J. Wang, I.J. Beyerlein, Atomic structures of symmetric tilt grain boundaries in hexagonal close packed (hcp) crystals, *Modell. Simul. Mater. Sci. Eng.* 20 (2012) 1–22, <https://doi.org/10.1007/s11661-012-1177-6>.